UNIVERSITY OF CALGARY

Fiber-taper collected photoluminescence characterization of diamond microdisks

by

Tamiko Masuda

A THESIS

SUBMITTED TO THE FACULTY OF GRADUATE STUDIES

IN PARTIAL FULFILLMENT OF THE REQUIREMENTS FOR THE

DEGREE OF MASTER OF SCIENCE

GRADUATE PROGRAM IN PHYSICS AND ASTRONOMY

CALGARY, ALBERTA

May, 2018

© Tamiko Masuda 2018

Abstract

A key architectural element of future quantum photonic networks is an efficient light-matter interface to connect electronic and photonic qubit systems. Nanophotonic resonators can be fabricated on-chip to provide such interfaces for atomic-like defect centers in diamond, which are leading qubit candidates. Fabrication advancements have recently lead to the construction of high quality diamond microdisk resonators, which show potential to reach enhancements with Purcell factor $C_{NV} \sim 50$. Here, a room-temperature experimental apparatus integrating free space and visible wavelength fiber-taper measurement capabilities is built to characterize diamond microdisk resonators. Using this setup, microdisk wisphering gallery modes with quality factors at visible wavelengths resonant with defect centers as high as $Q \sim 1 \times 10^5$, are observed for the first time. Spectral filtering effects of the taper on the microdisk are analysed to reveal that coupling to these disks may be limited by phase matching requirements. By thinning these disks it should be possible to improve coupling while lowering mode volumes, as desired to optimize Purcell factors.

Acknowledgements

I have been very fortunate to learn under the supervision of Dr. Paul Barclay, whose impressive knowledge and love of physics give our lab a strong backbone. I am ever so grateful for his encouragement and support. The opportunities he provided me with, such as attending CLEO and training in nanofabrication, have truly placed me among the most fortunate of students and I am very thankful for this investment and belief in me. He has given me direction so that I could grow, but also left the space so I could find myself as a researcher. Thank you.

With regard to those who helped me in the lab, I cannot in good conscience name any one of them before the others. Thus, by alphabetical order thank you to Behzad Khanaliloo, David Lake, JP Hadden, Matthew Mitchell and Thomas Lutz. Thank you for help with fiber pulling, for answering my questions and for all general support. Thank you to JP for the great amount of time spent helping me understand the setups, working to align optics, and pioneering the tri-acid cleans. Thank you to Behzad, David and Matt for making the devices I tested. I appreciate that this has been no easy task and it has earned my deepest gratitude. Thank you again to Matt and Dave for training me in Edmonton and for their endurance this past year, in fabrication.

I am grateful to Chris Healey, Hamid Kaviani, Ghazal Haji Salem, Gusatvo Luiz, Marcelo Wu and Prasoon Kumar Shandilya for bringing support, diversity and energy to our group. In addition, I thank Todd Willis and Darren Gisby in the workshop for turning my designs into creations and for their patience with my project. Thanks also to Jake Davidson, for always smiling.

Last but not least, I am grateful and appreciative of my family and friends, who have supported me throughout the years. Their love and encouragement empower me to follow the paths I desire.

Table of Contents

List of Tables

List of Figures and Illustrations

List of Symbols, Abbreviations and Nomenclature

Symbol	Definition
PSB	Phonon sideband
ZPL	Zero phonon line
FSR	Free spectral range
Q	Quality factor
$\mathscr{F}$	Finesse
Γ	Emitter loss rate
ξ	Taper-microdisk coupling factor
κ	Cavity loss rate
$a_{cw(ccw)}$	Clockwise (counter clockwise) traveling microdisk mode amplitude
$a_{c(s)}$	Symmetric (antisymmetric) standing wave microdisk mode amplitude
C	Purcell Factor
g	Emitter-photon coupling rate
η	Scaling factor of g based on diple moment position and orientation
ζ_{zpl}	Debye Waller factor for the ZPL
Θ	Scaling factor due to emitter-cavity detuning
S	Huang Rhys factor

Preface

Before delving into the formal aspects of my research, I would like to take a moment here to overview a more practical story of my Master's career. The purpose of this is to give the reader context for the work from my perspective as a student in the lab, to be juxtaposed with its context in the research community. Hopefully this will help to explain the effort invested in this project, which cannot be easily conveyed through final results.

The research in our lab revolves largely around the study of nanofabricated devices in dielectric materials and that of color center emitters in diamond. When I arrived in the lab our device fabrication, which is performed at the National Institute of Nanotechnology (NINT) in Edmonton, was already established. Experiments involving telecom optomechanics were being pursued by Matthew Mitchell and David Lake. Our postdoc JP Hadden, who had studied Nitrogen Vacancy (NV) centers at the University of Bristol, was hired just months before me to pursue emitter investigations.

Having discussed research options with Paul, I wanted to investigate coupling between the visible-wavelength optical resonances of diamond microdisks and color centers, potentially for application in a quantum memory. Realization of this coupling would be one way to bridge the research of our nanodevices with that of color centers. Upon my arrival I was very fortunate that there were several diamond devices already fabricated for optomechanics testing that were no longer in use by others. I could use these to begin.

Originally we expected that observing coupling between diamond microdisks and NVs would be quite straightforward. I began shadowing JP to understand the existing *Cryostat* setup, which has confocal free-space capabilities to study NV emission either at room or cold temperatures. We were able to see NV emission, however there was no signature of it coupling to the devices.

I then switched to characterizing the microdisks using transmission measurements, to check that good visible-wavelength optical modes existed and to see if any dependence on the microdisk

size could be found. I performed these measurements first using an existing fiber taper in the cryostat, and when that did not work, I measured them again on our *Ambient* setup. This setup has easier control of the fiber, but no free-space optics. The measurements at visible were somewhat cumbersome and though resonances were found, I was unable to draw conclusions on the quality our devices with respect to geometry. Difficulties with fiber measurements on both setups, which worked well at telecom wavelengths, were attributed to the fact that both fiber taper probes were made for telecom coupling. This resulted in less-than-optimal coupling at visible wavelengths. However, fiber tapers are very difficult to make and easy to break, so we could not temporarily exchange a telecom fiber taper for a visible one. Having a third and unused setup in the lab, I made a visible fiber taper with the aid of Paul Anderson, and mounted it there. Unfortunately, I could not get the fiber working properly in that setup.

Around this time it was decided that building a new and functional visible fiber taper setup would be the wisest course of action. We wanted both the capability of free-space emitter excitation as well as fiber taper collection. I spent significant time trying to think of a design to meet all our requirements, with valuable input from both Paul (Dr. Barclay) and JP. In addition to purchasing from vendors, I designed custom pieces - the most important of which are based off designs by a previous postdoc, Harishankar Jayakumar. I also composed an AutoCAD design for the full setup, to ensure all parts were compatible. The interative process of brainstorming, designing, re-evaluating, purchasing and talking to the science workshop spanned over a few months. The setup then got delayed by a workshop shutdown. Originally set to take about a month, the shutdown resulted in a 6-7 month gap between design submission and the start of machining.

In parallel with setup design and waiting for the workshop to be back on track, I continued trying free-space measurements with different device samples. In one case I managed to get what appeared to be a device-coupled NV signal using an NV-implanted electronic grade device. Electronic grade diamond chips have lower NV density than optical grade, but as they are $10\times$ the cost, we have very few of these fabricated. This lower density presumably removed some of the signal

from un-coupled NVs, opening an opportunity for measurement.

Alongside this I invested time in other areas regarding both device and emitter, which I hoped could be integrated in the project. In particular, I began to work with Thomas Lutz, JP and David, to consider silicon vacancy (SiV) centers and their implantation - a process used to obtain the color center of interest at a desired concentration and sample depth. Thomas had recently begun studying the SiV, which was showing great promise in the research community for its narrow linewidths. I was involved in measuring samples and preparing them for implanation. I furthermore put significant time into getting trained for fabrication, since devices had not yet been made specifically for optimizing visible wavelength coupling. Unfortunately timing has not yet allowed me to fabricate usable devices.

In addition to these efforts, I trained with JP on our tri-acid and phirana cleans. In preparation for device treatments, sample implanation, or fabrication, these cleans are very important to the health of our devices. Thus, while this time did not see a significant amount of measurement for me, I was quite invested in obtaining skills necessary for the general scope of the project.

By the end of summer in my second academic year, the setup was finally coming together. Into the fall of 2017 I was setting up, aligning optics, troubleshooting setup concerns, pulling fibers and finally acquiring data. At this point, reasonable characterization could be done on the microdisks to gain an understanding of the system and what next-steps to make regarding fabrication. This thesis is focused on the measurements taken during that time.

Contributions

To conclude this preface, below I highlight how the work presented in this thesis is a result of contributions not just by myself, but my labmates.

Fabrication Devices I have tested throughout my thesis are thanks to fabrication efforts by Behzad Khanaliloo, David Lake, Matthew Mitchell and Aaron Hryciw. I did not fabricate the devices in this thesis.

Confocal PL A confocal PL setup on our cryostat setup was already established when I arrived. Many of the measurements I performed with confocal and off-axis confocal configurations, were done with JP Hadden. He also played a key role in training me to use the setup. In addition, Thomas Lutz helped me with free-space optics measurements and tips, though much of what we studied together is not included in this thesis.

New Setup In designing the setup I took much inspiration from existing setups in the lab and from designs of Harishankar Jayakumar. JP aided me significantly through the process of choosing and designing pieces. We spoke quite often on my ideas and their feasibility, and he answered many of my questions regarding the setup. With regard to ordering and other general questions I had further discussion and ideas from Matthew and David. The purchasing, design drafting, vendor and workshop communication, and setup construction was primarily completed by myself.

Fiber pulling Fiber pulling has been a group effort. I have pulled fibers, along with the aid of JP Hadden, David Lake, Matthew Mitchell, Behzad Khanaliloo, Prasoon Kumar Shandilya and Paul Anderson.

Simulation I ran FDTD simulations, with help from previous MEEP and Matlab scripts that were in some combination from David Lake, Chris Healey and Paul Barclay.

Fiber Taper measurements Matt, David and JP all helped me to get acquainted with fiber taper measurements to some extent. However, the majority of visible taper measurements that I have taken and much of the troubleshooting to see visible signals, was done by myself.

Fiber-collected PL I performed the fiber collected PL measurements primarily alone, but with much assistance especially in spectrometer alignment from JP Hadden.

Publications and presentations

M. Mitchell, B. Khanaliloo, D. Lake, T. Masuda, J.P.E. Hadden, P.E. Barclay, Single crystal diamaond low-dissipation cavity optomechanics, Optica 3, 963-970 (2016)

T.Masuda, J.P.E Hadden, D. Lake, M. Mitchell, and P.E. Barclay. Fiber-taper collected photoluminescence characterization of diamond microdisks. (In progress).

May 18, 2017, T. Masuda, M. Mitchell, B. Khanaliloo, D. Lake, T. Lutz, J.P.E. Hadden, W. Tittel and P. E. Barclay. High-Q diamond microdisks for coupling to SiV quantum emitters (contributed), Conference on Lasers and Electro-Optics (CLEO), San Jose, USA May 14-19 2017

Chapter 1

Introduction

Quantum networks could provide the hardware needed to tap into computational and communicative powers off limits to classical counterparts, for realization of quantum computing, communication and cryptography[1]. At the heart of such a network are quantum bits that do not interact with their environment (decohere), yet do allow access for manipulation upon command[2]. In practice it is challenging to find physical systems to meet these seemingly contradictory requirements, but one promising framework is a quantum *photonic* network. This elects photons for robust transport, employs atomic-like systems for state accessibility, and bridges the two with light-matter interactions[3, 4].

Among leading solid-state candidates for the atomic-like qubit in such a platform are defects in diamond (e.g., impurities and vacancies) known as "color centers", owing to their ability to emit light. These defects have demonstrated building-block phenomena for quantum networks, including entanglement[5, 6, 7], teleportation[8], indistinguishable single photon generation[9, 10] and optical switching[7]. However, the success rate of spin-spin-entanglement based protocols are often limited by emitter properties as well as poor collection at the diamond-air interface, which affect the detection of coherent photons in a heralding measurement. In particular, Bernien *et al.*[5] estimated a rate of $\sim 10^{-7}$ successes per entanglement generation attempt, and longer-distance entanglement[1] performed by the same research group, Hensen *et al.*[11], had 6.4×10^{-9} successes per attempt. These rates can be improved by manipulating the emitter-photon interaction with efficient interfaces. In other words, by engineering optical cavities that modify the emitter's spontaneous emission to enhance the rate of coherent photon generation. Furthermore, if the cavity-emitter system is able to operate in the strong coupling regime, where the emitter-photon coupling rate exceeds both the emitter and cavity decoherence rates, it could be exercised as a quantum

[1] famously used to perform a loop-hole-free Bell inequality violation of great significance to fundmanetal physics

interconnect and gate[3].

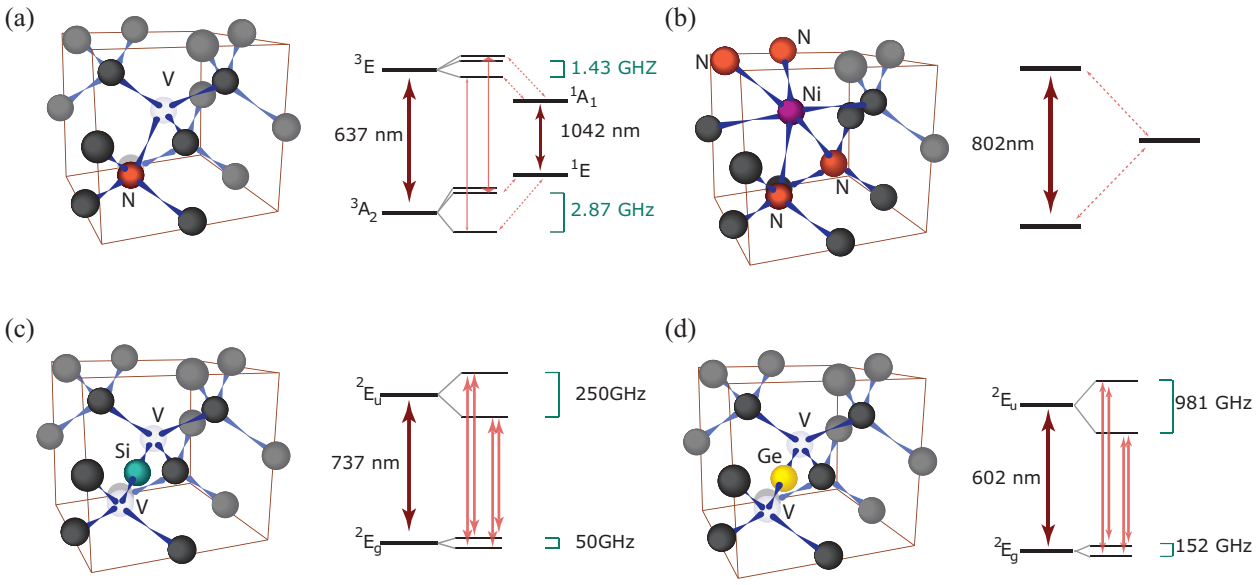

Figure 1.1: (a) The NV[12] exhibits a C_{3V} symmetry with a ground state orbital singlet A_2 and excited state doublet, E, both spin triplets. The degeneracy between $m_s = \pm 1$ and $m_s = 0$ states is lifted (at zero-applied-field) due to crystal field splitting. Non-radiative decay through an inter-system crossing provides the NV with spin-dependent flourescence. (b) The NE8[13] has a C_{2h} symmetry and composed of a Ni atom bonded to two N and two C atoms. There is no vacancy. While the orbital states are not known, it is a $s = \frac{1}{2}$ system. (c) SiV[10] and (d) GeV[14] centers comprise of an interstitial impurity atom between two vacant lattice sites. This creates an inversion-symmetric potential, thus removing the first-order permanent dipole moment and nearly eliminating effects of spectral diffusion. They have a D_{3d} symmetry, with doublet E_g ground and E_u excited states, which are again both spin doublets ($s = \frac{1}{2}$).

For an ideal two level system the weak-coupling ("Purcell") enhancement of photon emission is independent of emitter properties and scales only by Q/V for cavity quality factor Q and mode volume V. The same cannot be said of the realistic diamond defect centers, which can demonstrate different enhancements in the same cavity, based upon their individual properties. Thus, both the enhancement of coherent photon generation and the intrinsic photon emission rate will be dependent on the selection of a color center. That said, the desired application will dictate which center is used. For example, on-demand single photon sources beg for bright emitters that can produce identical photons with a fast generation rate - spectrally such an emitter would have a narrow linewidth. On the other hand, operations requiring a quantum memory demand that the

emitter can also function as a spin qubit with long coherence times to maintain fidelity of a state, on a timescale comparable to or longer than quantum operations. Although diamond has numerous optically active defects [15], only a handful of these have been investigated in detail. Figure1.1 depicts structures of some of the more well-known color centers.

To-date the negatively charged nitrogen vacancy (NV^-) center (Fig.1.1(a)) has been most studied. It is famous for long room-temperature spin coherence times of 1.8ms[16] in the electronic ground state, which can be coupled to nuclear spins of even longer coherence times for quantum memories[17]. Unfortunately it also possesses a permanent dipole moment that results in spectral diffusion, creating inhomogenous broadening that is detrimental. It also emits only 3% of its photons through the (coherent) zero-phonon-line (ZPL) transition[12], which largely impairs success rates mentioned earlier.

In contrast, the silicon vacancy (SiV) and germanium vacancy (GeV) centers (Fig.1.1)(c),(d)) have vanishing permanent dipole moments, narrow linewidths, and emit roughly $\sim$70%[18] and $\sim$60%[19] into their ZPLs respectively. This positions them as superior candidates for single photon protocols than the NV, though with far less impressive spin coherences of 115ns[20] and 19ns[21], for the SiV and GeV respectively, at low temperatures. Both demonstrate strong spin orbit coupling with a resultant zero-field splitting that lifts orbital degeneracies, providing useful Raman transitions[7].

Color centers containing transition metals have also been investigated. For example, the NE8 center (Fig.1.1(b)) is known to exhibit narrow linewidths, but has been more challenging to implant[22] than the SiV. Another example is the collection of chromium-related defects, several of which were created via chemical vapor deposition (CVD) growth and studied by Aharonvich *et al.*[23]. The defects showed emission between 740nm - 770 nm, lifetimes 1-14ns and had both two and three level energy structures, of linewidths $\sim$ 10nm and $\sim$ 4nm repsectively. Aharonvich *et al.* later implanted one such center, and proposed it to have an interstitial Cr geometry[24].

As this quick summary of diamond defects showcases, it is difficult to find an emitter that is

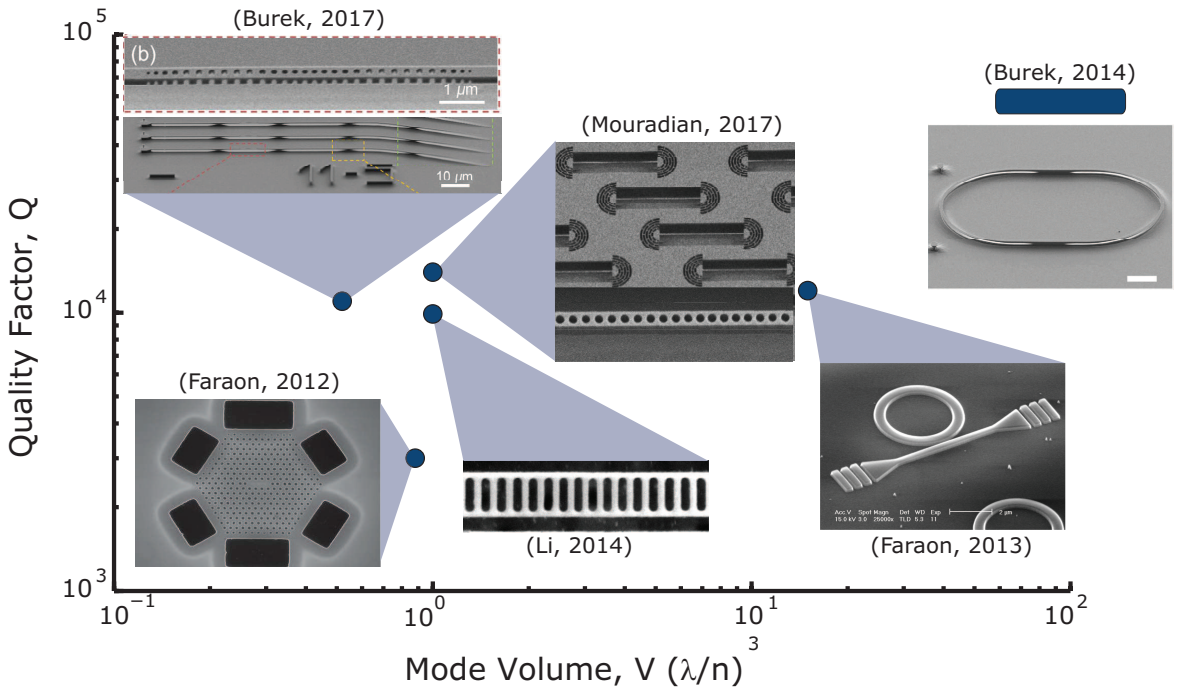

Figure 1.2: A summary of the quality factors and mode volumes of some of the best visible-wavelength diamond devices. To optimize coherent photon generation movement towards the top left of the graph is desired. References:[25, 26, 27, 28, 29, 30]. Note that mode volume of the racetrack resonators(Burek,2014)[27] were not reported and has been placed at very rough range of V, estimated from device dimensions.

ideal in every regard. Thus future diamond platforms may very well incorporate several of these emitters for various application. To capitalize on the properties of each an efficient light matter interface is beneficial. Cavities can help to utilize the NV spin while improving the generation of ZPL photons; they can enhance generation of single photons from promising emitters such as the SiV; and if both cavity and emitter loss rates , κ and Γ respectively, can be made such that they are much less than the emitter-photon coupling, $g \ll \kappa, \Gamma$, the realization of, e.g., the CNOT gate may be possible.

Thus, a push towards quantum networking in diamond requires careful consideration of the cavity used to promote emitter-photon interactions. On-chip realizations of these interfaces amount

to nanoscale optical resonators in dielectric materials. Generally, there are two ways to achieve this: fabricate devices from non-diamond materials ("hybrid" devices) and couple to a color center housed outside the device; or make the device from diamond with the emitter inside.

The first nanodevices constructed for coupling to color centers were hybrid devices atop bulk diamond[31, 32, 33]. However, the optical modes of such devices live primarily inside the device and hybrid systems therefore cannot place the emitter at the maximum electric field where optimal emitter-photon interactions would occur. That said, the realization of devices in diamond was intially stunted by fabrication barriers presented by its poor heteroepitaxial growth[27]. This prevented the community from being able to fabricate high-quality diamond membranes using standard fabrication techniques. Only recently have such challenges been circumvented by the development of innovative bulk single crystal diamond techniques, namely, thinned membranes[34], angled etching[35] and quasi-isotropic undercut etching[36].

Single crystal diamond (SCD) ring resonators[34, 28], photonic crystals[25, 7, 30, 26] and racetrack resonators[27], have been studied over visible wavelength ranges that include color center optical transitions. Figure 1.2 provides a visual comparison of the Q and V of few of these devices. It should be noted that here Q relates to the storage of energy in an optical mode, while V describes a mode "volume" in which the electric field is concentrated (cf. Section2.2.3) and can be linked directly to the per-photon electric field strength. To improve emitter-photon coupling it is advantageous to obtain high Q and low V. Racetrack devices hold the highest published visible-wavelength quality factor[27], Q $\sim 6\times10^4$, of SCD devices but have $\sim 10^2$ wavelength circumferences that suggest mode volumes of similar order. Photonic crystals have been demonstrated with more moderate Q$\sim 1\times10^4$, but showcase record-low[25] mode volumes of $<(\lambda/n)^3$. Ring resonators have moderate Q$\sim 3\times10^4$ as well as mode volume, V$\sim 10^1(\lambda/n)^3$.

In this thesis I present a spectroscopic study of SCD microdisks with simulated mode volumes $\sim 10^1(\lambda/n)^3$ and measured quality factors as high as 1×10^5, at wavelengths in range of color center transitions. These microdisks are fabricated by the quasi-isotropic undercut technique pi-

noeered by my labmates[36], which is highly repeatable and therefore provides advantage over others for future platform scaling[26]. The study will exploit the fact that optical grade SCD chips have a high intrinsic density of NV centers, which emit over roughly 200 nm, to study these devices via fiber-collected NV phonon sideband (PSB) photoluminescence (PL). Using the NVs as an internal microdisk light source allows measurement over several cavity free spectral range (FSR). This broadband spectrscopy is supplemented by tunable-wavlength laser transmission measurements that have higher resolution, but narrower range (5 nm).

I will begin this thesis by introducing relevant background theory on microdisks and their measurement with fiber tapers (chapter 2). Next, I will provide an overview of the Purcell enhancement first in the most ideal case and ending with the situation relevant for the measurements performed here (chapter 3). As to achieve this measurement required the construction of a new setup, I will speak on the setup design and reasons why it was necessary (chapter 4). Finally, the fiber-based microdisk spectroscopy and analysis will be considered (chapter 5).

Chapter 2

Microdisks

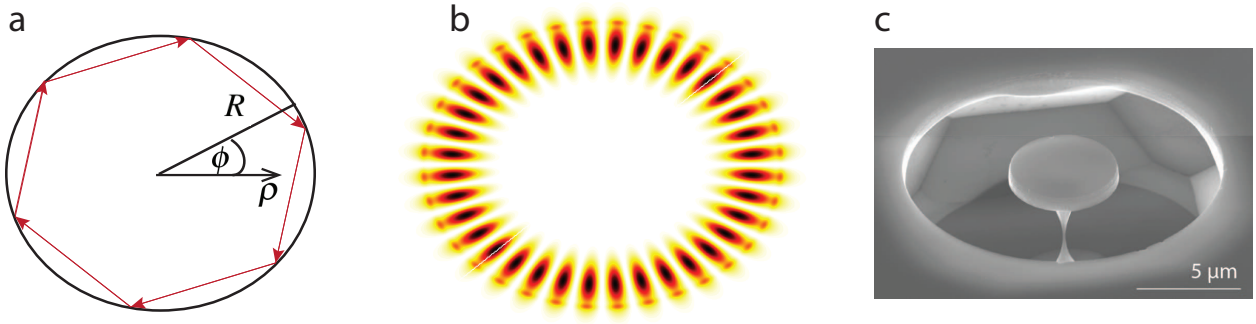

Figure 2.1: (a) Ray diagram of confinement in a microdisk of radius R.(b) Electric field profile in the $\rho - \phi$ plane for a fundamental mode, simulated by FDTD, *plotted by: David Lake*. (c) SEM of an example diamond microdisk, *credit: Matthew Mitchell*.

Microdisks are thin cylindrical devices fabricated from dielectric materials. In the most basic picture, the confinement of light in these structures can be thought of as total internal reflection of a ray guided inside the high refractive index disk (Fig.2.1(a)). The electromagnetic picture is a wave following a circular trajectory around the circumference of the microdisk, i.e. that obeys periodic boundary conditions. Fig.2.1(b) displays the simplest of microdisk mode electric field profiles, which hug the periphery of the microdisk and are known as whispering gallery modes (WGM). In diamond, an example of the devices studied in this thesis is given in Fig.2.1(c), where it is clear that in reality the microdisks are supported by a thin pedestal.

In this chapter I first briefly discuss the approximate analytic microdisk mode solutions to Maxwell's equations, summarizing key points to afford intuition. The notes follow derviations made in the thesis of Borselli[37], to which I refer the reader for further detail. Next, I will define basic parameters and figures of merit that will be important in our later discussion of the devices. Finally, I will summarize important points on fiber-taper coupling to microdisks, largely

in reference to Borselli[37] and Srinivasan[38], as needed to understand the characterization later in this thesis.

2.1 Approximate solutions

Rigorous analytic solutions to Maxwell's equations for the optical modes of microdisks do not exist, however, to gain some perspective on mode profiles through analytic means we can make several approximations. To do so one can begin with the charge-free, current-free formulations of Maxwell's equations and assume that (1) the index of refraction is independent of the azimuthal direction, $n(\bar{r}) = n(\rho, z)$, and (2) the medium is piecewise homogeneous. It is then possible to arrive at the Helmholtz equation, which in cylindrical coordinates is:

$$\bigtriangledown^2 F + k_o^2 n^2(\rho, z) F(\bar{r}) = 0 \tag{2.1}$$

where here $F = \{E, H\}$ for electric (E) and magnetic (H) fields with free space wave number $k_o = \omega_c / c$.

The next assumption is rather important. We wish to enforce solutions to take purely transverse electric (TE) or magnetic (TM) polarizations. These modes are defined by electric and magnetic field components *parallel* to the *disk plane*, respectively. As claimed in [37] this is valid for disk thicknesses larger than $\lambda_c/(2n)$. Separation of variables can then be applied twice over to obtain ODEs for the components of our field in the case $\rho < R$:

$$\begin{aligned} \frac{\partial^2 Z}{\partial z^2} + k_o^2 (n^2(z) - \bar{n}^2) Z = 0 \\ \frac{\partial^2 \Omega}{\partial \phi^2} + m^2 \Omega = 0 \\ \frac{\partial^2 \Psi}{\partial \rho^2} + \frac{1}{\rho} \frac{\partial \Psi}{\partial \rho} + (k_o^2 \bar{n}^2(\rho) - \frac{m^2}{\rho^2}) \Psi = 0 \end{aligned} \tag{2.2}$$

with effective index $\bar{n}$ and Z, Ω, Ψ the vertical, azimuthal and radial functions, respectively. The first ODE gives modes for slab waveguides [37, 39], the next provides an $e^{im\phi}$ dependence, where m defines the mode's angular momentum and must take an integer value to satisfy periodic boundary conditions. The last ODE in Eqn.2.2 will give Bessel functions inside the microdisk, and

furthermore employing boundary conditions it is possible to obtain the radial dependence:

$$\Psi(\rho) \sim \begin{cases} J_m(k_o \bar{n} \rho), & \rho \leq R \\ J_m(k_o \bar{n} R) e^{-\alpha(\rho - R)}, & \rho > R \end{cases} \tag{2.3}$$

where J are bessel functions, α is defined as $\alpha = k_o(\bar{n}^2 - n_o^2)^{1/2}$, R is the microdisk radius and the exponential in the latter case is approximation to a Hankel function.

Intuitions are solidifed by these results. Namely: (a) with our assumption of thin microdisks the maximum field is vertically in the center as according to slab waveguide calculations; (b) we have a dependence of $e^{im\phi}$; (c) outside the microdisk the mode will decay with constant α such that higher index microdisks show tighter confinement.

After all these assumptions it should be reinforced that the true solutions are not perfectly TE or TM. In reality the modes are TE (TM)-*like* hybrid modes, but for simplicity these will be referred to as"TE" ("TM"), based upon which ever polarization has the highest field concentration. Furthermore, in the microdisks studied here it is possible to observe vertical order modes, therefore the solutions will be grouped into families of radial order p and vertical order q, here labeled TE (TM)$_{p,q}$. Note that enforcing these polarizations has caused us to neglect a longitudinal (E_ϕ) component of the field. With a more rigorous definition of TE and TM defined instead by parity across the vertical mirror plane the solutions can always be grouped in to TE and TM. As with the derivation in this section, I refer the reader to Borselli[37] for further discussion.

2.2 Cavity property definitions

In order to address emitter-photon coupling, this thesis is primarily focused on consideration of the Purcell effect. For an ideal emitter the Purcell factor $C \sim Q/V$. Therefore, in this section I will discuss the defintions of both Q and V independently so their importance for photon coupling is more evident. Sometimes in the literature the finesse, $\mathscr{F}$, is used in place of Q to evaluate Purcell enhancements. Therefore I will also very briefly touch on the differences of the two for understanding, though $\mathscr{F}$ will not be seen here beyond its introduction.

2.2.1 Quality factor

As alluded to by the nomenclature, a high quality resonator has a high quality factor. Specfically, this "quality" refers to how long energy is stored in a mode of resonant frequency ω_c. It is defined[37]:

$$Q = \omega_c \frac{\mathscr{E}}{P}. \tag{2.4}$$

Here $\mathscr{E}$ is the stored energy and $P = d\mathscr{E}/dt$ is the power dissipated by the cavity. By power conservation one can solve for $\mathscr{E}(t) = \mathscr{E}_o e^{-\omega_c t/Q}$, and immediately read off the cavity decay rate: $\kappa = \omega_c/Q$. The corresponding photon lifetime or "confinement" time is then given as $\tau = 1/\kappa$. Taking the derivative of $\mathscr{E}(t)$, we can use $|P| = \mathscr{E}/\tau$ to rearrange eqn.2.4 as:

$$Q = 2\pi \frac{\tau}{\tilde{T}}, \tag{2.5}$$

which allows us to reinterpret Q as $2\pi\times$ the confinement time expressed in units of the optical period, $\tilde{T}$[40].

The cavity material and design affect confinement time. For example, high refractive index contrast between a microdisk and its surrounding medium can assist with prolonging confinement. The related loss results from radiation to the continuum of free-space modes and is associated with the radiative quality factor, Q_{rad}.

In reality the total Q of a device will suffer further losses that reduce confinement time. In particular, surface roughness[41] and impurities[42] are realisitcally present in any nanofabricated device to some extent, though this may be controlled to some degree by the fabrication procedure. Like in [42], the diamond microdisks in this thesis are prepared by a series of etches, where lattice damage from an etch could result in impurties and defects on the surface, in addition to physical roughness. These result in surface scattering and absorption losses that I will associate with Q_{fab}. In addition there may be scattering or absorption in the bulk material itself[42], which I will relate to Q_{bulk}.

Measurements in this thesis are done via fiber taper probe and the presence of the taper waveguide will create an additional loss channel, associated with Q_{taper}. As loss rates add directly,

quality factors are added in parallel. Explicitly

$$\begin{aligned}\frac{1}{Q} &= \frac{1}{Q_{rad}} + \frac{1}{Q_{fab}} + \frac{1}{Q_{bulk}} + \frac{1}{Q_{taper}} \\ &= \frac{1}{Q_i} + \frac{1}{Q_{taper}}.\end{aligned} \tag{2.6}$$

The first terms in eqn.2.6 have been grouped into Q_i, the intrinsic quality factor, which tells us how the system is limited without our probing waveguide. Q as defined above, including the fiber contribution is known as the *loaded* quality factor.

2.2.2 Finesse and FSR

Any standard optics textbook, e.g.[39], will define the following three quantities. First, the free spectral range (FSR), which represents the spectral separation between modes with azimuthal quantum numbers m and $m+1$ of the same (p,q) family:

$$FSR_\Theta = |\Theta_{m+1} - \Theta_m|, \tag{2.7}$$

where $\Theta = \{\omega, \lambda, \nu\}$. Second,the group velocity, which describes the velocity of a packet of light (speed of energy transfer):

$$v_g = \frac{\partial \omega}{\partial \beta}, \tag{2.8}$$

where β is the propagation factor of the mode. Third the finesse, $\mathscr{F}$:

$$\mathscr{F} = \frac{FSR_\omega}{\delta\omega} \tag{2.9}$$

with $\delta\omega$ the resonance's FWHM. Borselli[37] awards us some intuition on $\mathscr{F}$, by relating $\beta = m/\rho$ such that $v_g \sim FSR_\omega R$. This gives a round trip time of $\tau_{RT} \sim 2\pi/FSR_\omega$ that allows us to rewrite the finesse:

$$\mathscr{F} = 2\pi\frac{\tau}{\tau_{rt}}. \tag{2.10}$$

In other words, while Q is $2\pi\times$ photon lifetime in optical periods, $\mathscr{F}$ is it in units of round-trips.

2.2.3 Mode volume

We can increase emitter-photon interactions in two ways, either (1) keep photons in the cavity long enough to be absorbed by the emitter, or (2) make the photon field stronger in the vicinity of the emitter. The quality factor addresses point (1), while mode volume addresses point (2). The effective mode volume, V, describes the concentration of the electric field, by dividing the total electric field energy by its maximum[37, 38]:

$$V_{eff} = \frac{\int |\mathbf{E}(\mathbf{r})|^2 \bar{n}^2(\mathbf{r}) dV}{max\big(|\mathbf{E}(\mathbf{r})|^2 \bar{n}^2(\mathbf{r})\big)} \tag{2.11}$$

Thus, the ideal device will have high Q and a low V. Optimization commands a balance between the interplay of Q and V, as smaller devices inherently have smaller V but will suffer increasing radiative losses and, likely, fabrication losses.

2.3 Simulation

To gain perspective on the cavity mode spectrum for a given device geometry and to predict V, it is useful to turn to numerical simulations. This thesis uses finite difference time domain (FDTD) simulations performed with the program MEEP. All technical details that I will refer to in this chapter can be found in the manual[1]. FDTD simulations evaluate a quantity (here the electromagnetic field), as propagated over a mesh grid of discrete distance points (Δx) and through discrete time points (Δt) with the evolution dictated by relevant differential equations (here Maxwell's equations). These are limited largely by the resolution chosen, since one uses $\Delta t, \Delta x$ to approximate infinitesimal steps. Unlike the analytic approximation, the simulations do not restrict TE or TM polarization, so fields will be hybrid in nature and also may have a vertical order.

MEEP uses dimensionsless units. c is set to 1 and the user must define a length scale, a that distances will be measured in. For example, if $a = 1\ \mu$m, then $\lambda_c = 737$ nm would become $0.737a$. The resolution you set with MEEP is the number of pixels per a. For a resolution 40 and $a = 1$ used in simulations here, $\Delta x = 25$ nm.

[1] https://meep.readthedocs.io/en/latest/Introduction/

Since $c = 1$, frequency and time units become $[\nu] = [1/a]$ and $[t] = [a]$, respectively. The resolution in time is given by $\Delta t = S\Delta x$. As set by MEEP, $S = 0.5$. S is the courant factor and to be stable, $S < n_{min}/\sqrt{\#dim}$. Since the minimum index of refraction is often 1 (also the case for us), $S = 0.5$ is valid for all three dimensions.

We can exploit the rotational symmetry of microdisks by performing only a 2D simulation and obtain 3D results. This amounts to using cylindrical dimensions in MEEP and assigning "no size" to the size of ϕ. MEEP will ensure that the solutions have an $e^{im\phi}$ dependence for a user-set (integer) m, which indirectly meets the requirement of periodic boundary conditions. One defines the geometry of the device - here a cylinder of diamond surrounded by air - and then creates a source inside, to excite the optical modes. Using a pulse that is gaussian in time with some defined bandwidth, df, we are able to determine the frequency range of the resonances that we want to evaluate. In the simulations here, for the cylinder positioned with the center at (ρ,z)=(0,0) I placed a E_r-polarized gaussian source centered at (ρ,z)=($\frac{4}{5}R$, $\frac{3}{10}h$). Being off center in both ρ and z, but stimulating with the E_r source, allowed for modes of both TE and TM polarization to be evaluated at once, owing to the presence of this field component in both TE and TM modes away from the vertical mirror plane. That said, because of the source polarization, TE modes were more strongly stimulated than TM modes.

Using the built-in function *harminv* MEEP outputs mode center frequency and quality factor by fourier transforming the temporal evolution of the excited field and analyzing its spectral features. First using a broadband source (e.g., df=0.5), one can find resonance locations. To confirm the type of mode and get an accurate value of Q one must then run a narrower bandwidth around the resonance frequency of interest (e.g.,df=0.01). From the field output of the narrowband case, we can plot fields to determine which electric field component is the largest and assign it a polarization as such.

In addition to being able to visualize mode profiles and get a radiative Q estimate, these simu-

lations allow us to evaluate FSR and mode volume. Approximately we expect that FSR follows:

$$FSR_\lambda = 2\pi R\bar{n}(\frac{1}{m_1} - \frac{1}{m_2}) \tag{2.12}$$

To get an estimate of the FSR range, in the simplest case one can replace $\bar{n}$ with the index of refraction of diamond, n_d. A more accurate estimation can be obtained by replacing $\bar{n}$ with a reduced effective index that accounts for the fraction of the mode that exists in the air region. This can be a guideline when searching for higher order modes of the same (p,q) family in simulation, or when trying to identify the families in measurement. Simulated mode profiles must be checked to ensure that both resonances belong to a family of same polarization as well as (p,q).

Mode volume is evaluated by the output file of electric field, E by calculating:

$$V = \begin{cases} 0.5\frac{\mathscr{E}_{tot}}{\max(|E_z|^2+|E_\rho|^2)}\left(\frac{n_d}{\lambda_c}\right)^3, & |E_\phi^{max}|^2 > |E_z^{max}|^2 + |E_\rho^{max}|^2 \\ 0.5\frac{\mathscr{E}_{tot}}{\max(|E_\phi|^2)}\left(\frac{n_d}{\lambda_c}\right)^3, & \text{else} \end{cases} \tag{2.13}$$

where

$$\mathscr{E}_{tot} = \sum_i \sum_j \left(n_{i,j}E^2_{T(i,j)}\right) 2\pi\rho_i\Delta\rho\Delta z \tag{2.14}$$

and $\Delta\rho = \Delta z = \Delta x$. i and j correspond to grid indicies along the ρ and z directions, for all the various quantity outputs. The mode volume is scaled to be in units of the $(\lambda_c/n_d)^3$. When simulating these modes we make an assumption that we are studying standing waves, which require the conditionals in Eqn.2.14 as well as the factor of 1/2. More details on this can be found in[37].

2.4 Coupling to microdisk modes

Nanophotonic devices are often characterized by transmission measurements using waveguides. A fiber taper probe can provide waveguide with autonomous positioning without the fabrication challenges of on-chip waveguides. These probes consist of optical fibers that have been stripped of coating and thinned to provide a region where evanescent light can be used to couple to devices. The following discussion is focused on an understanding of fiber-taper transmission measurements and how these relate to cavity properties.

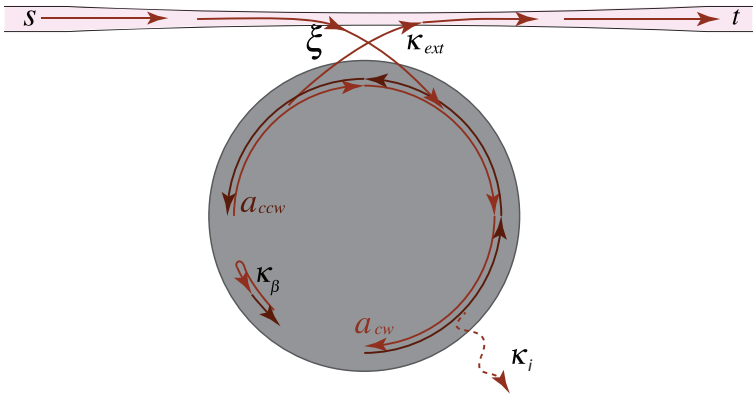

Figure 2.2: A signal with normalized input power $|s|^2$ is sent into the taper, coupling to a clockwise propagating mode, a_{cw}. A degenerate counter propagating mode a_{ccw} may couple via backscattering with a rate κ_β. The cavity suffers an intrinsic loss rate κ_i and couples out of the system to the fiber with rate κ_{ext}. The transmitted signal is t.

To understand transmission measurements, the associated electric field amplitude and decay rates of the system are defined in Fig.2.2. Explicitly the fiber taper-microdisk coupling rate ξ is dependent on fiber-microdisk mode field overlap[37]

$$\xi = \frac{i\omega_c \varepsilon_o}{4}\left\{\int \delta n_c^2(r) E_c^*(r)\cdot E_f(r) dV + \int \delta n_f^2(r) E_f^*(r)\cdot E_c(r) dV\right\}. \tag{2.15}$$

Here c subscripts are for the cavity and f for the fiber. $E_c \propto e^{im\phi}$ and $E_f \propto e^{-i\beta_f \rho sin(\phi)}$ such that non zero coupling should occur when $m \sim \beta_f \rho$, with β_f the fiber taper propagation constant.

2.4.1 Traveling waves

Now following Srinivasan[38], relevant parameters in Fig.2.2 are related through an input-output formalism as:

$$\frac{da_{cw}}{dt} = (i\Delta\omega - \frac{\kappa}{2})a_{cw} + \xi s \tag{2.16}$$

where $\Delta\omega = \omega_c - \omega$, ω the driving frequency and κ the total loss rate:

$$\kappa = \kappa_i + \kappa_p + \kappa_{ext} \tag{2.17}$$

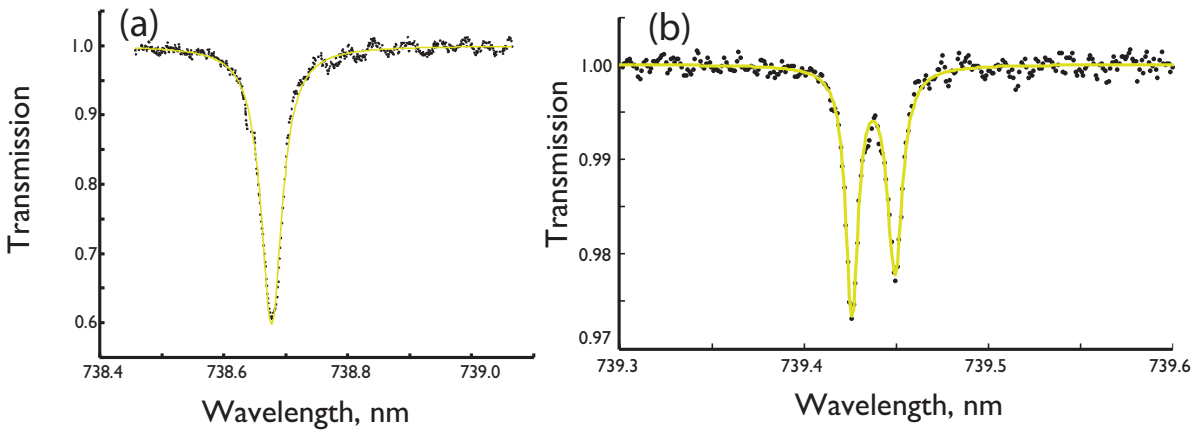

Figure 2.3: Transmission spectra from diamond microdisks via fiber taper probe. (a) Example of a singlet mode with ∼40% resonance contrast, representing a traveling wave. (b) Example doublet mode with <3% resonance contrast representing a standing wave.

The last two terms are due to the fiber taper, $\kappa_{taper} = \omega_c/Q_{taper}$, whose contribution has been split into losses coupling to the external waveguide, κ_{ext}, and those it induces which are lost from the cavity-taper system, κ_p, e.g. by scattering.

It can be shown that $\xi = \sqrt{\kappa_{ext}}$ [38], and if one employs once again power conservation arguments, then the transmission, $T = |t/s|^2$, for a transmitted signal t can be found:

$$T = \left| -1 + \frac{\xi^2}{i\Delta\omega + \kappa/2} \right|^2 \tag{2.18}$$

The signal is an inverted Lorentzian with width of κ. In practice, we measure a width $\Delta\lambda$ and calculate $Q = \lambda_c/\Delta\lambda$. An example of such a transmission scan is given in Fig.2.3(a) and represents a traveling wave with the signal referred to as a *singlet* mode.

2.4.2 Standing waves

In practice, imperfections in the microdisks can sometimes lead to *backscattering* inside that couples to the degenerate, backwards propagating mode, i.e., a_{cw} to a_{ccw} and vice versa. Now follow-

ing Borselli[37]:

$$\begin{aligned}\frac{da_{cw}}{dt} &= (i\Delta\omega - \frac{\kappa}{2})a_{cw} + i\frac{\kappa_\beta}{2}a_{ccw} + \xi s \\ \frac{da_{ccw}}{dt} &= (i\Delta\omega - \frac{\kappa}{2})a_{ccw} + i\frac{\kappa_\beta}{2}a_{cw}\end{aligned} \tag{2.19}$$

Both of these equations are written out in full to emphasize that light sent in through the fiber taper will only couple to one of the traveling modes, here labeled the clockwise mode. These equations are now coupled, but it is possible to decouple them by moving to a basis of the following superpositions, which represent standing waves:

$$\begin{aligned}a_c &= \frac{1}{\sqrt{2}}(a_{cw} + a_{ccw}) \\ a_s &= \frac{1}{\sqrt{2}}(a_{cw} - a_{ccw}).\end{aligned} \tag{2.20}$$

The decoupled equation of motion for the *symmetric (antisymmetric)* mode $a_c(a_s)$ is then:

$$\frac{da_{c(s)}}{dt} = \big(i\Delta\omega + i\frac{\kappa_\beta}{2} - \frac{\kappa}{2}\big)a_{c(s)} + \frac{1}{\sqrt{2}}\xi s \tag{2.21}$$

We then make the assumption that this equation still holds if generalizing to a case where κ is replaced by loss rates κ_c or κ_s to account for differing losses in the two standing wave modes. Steady-state amplitudes are then solved for:

$$a_{c,s} = \frac{-\sqrt{\kappa_{ext}/2}}{-\kappa_{c,s}/2 + i(\Delta\omega \pm \kappa_\beta/2)}, \tag{2.22}$$

with corresponding transmission

$$T = \left| -1 + \sqrt{\frac{\kappa_{ext}}{2}}(a_c + a_s) \right|^2 \tag{2.23}$$

The symmetric(antisymmetric) mode has linewidth given by $\kappa_{c(s)}$ and shifted by $\kappa_\beta/2$. Unlike the traveling waves, these standing waves are non-degenerate and result in two transmission dips. The standing wave resonances are referred to as *doublet* modes (Fig.2.3(b)).

2.4.3 Additional transmission notes

The minimum measured waveguide transmission, $T_{min} = T(\omega_c)$, is an important quantity to be aware of while measuring, because it indicates how well the taper and microdisk are coupled. One

may also refer the related resonance contrast, *RC*:

$$RC = (1 - T_{min}) \tag{2.24}$$

Sometimes, *RC* is referred to in percent, rather than as a ratio. It is an important quantity in that it relates the input power, P_{in} to the amount "dropped" into the cavity, P_d[37].

$$P_d = RC \times P_{in} \tag{2.25}$$

For a singlet, we can make sense of coupling regimes by considering[43]:

$$T_{min} = \left| \frac{1-K}{1+K} \right|^2 \tag{2.26}$$

where K is defined as:

$$K = \frac{\kappa_{ext}}{\kappa + \kappa_p} \tag{2.27}$$

If $K < 1$ we say the system is undercoupled, if $K > 1$ it is overcoupled and if $K = 1$ it is critcally coupled[43]. In a critically coupled case, all of input power is transferred to the cavity ($RC = 1$). These quantities are furthermore important when studying power-dependent wavelength shifts in the transmission spectra, but as these are not studied here, I refer an interested reader back to [37]. For all the measurements in this thesis, we are operating in the undercoupled regime.

Chapter 3

Cavity-Emitter coupling: the Purcell effect

When a cavity is constructed around an emitter, it changes the photon density of states available for that emitter to decay into and consequently alters the spontaneous emission rate. The Purcell factor, $C = \Gamma^{cav}/\Gamma^{fs}$, describes how spontaneous emission rate into a photonic mode of a cavity, Γ^{cav}, compares to the free space spontaneous emission rate, Γ^{fs}. In this chapter I discuss background relating to C.

Exactly what literature calls "the" Purcell factor can sometimes be confusing and even inconsistent. To be extremely clear of the defintions used in this thesis, I will be differentiating between the Purcell factor C and two special cases that lead to definitions of the *ideal* Purcell factor, C_δ, and *ZPL* Purcell factor, C_{zpl}. I will begin with the ideal case and then discuss some effects relating directly to the NV center. The relevance of these cases in the context of this thesis will be explained in each section.

3.1 Ideal case

We obtain the ideal Purcell factor for the case where our cavity decay is larger than our emitter's total free space spontaneous emission rate, $\kappa > \Gamma^{fs}$, and when the emitter behaves like a Dirac-function. For this reason I will label variables with δ. In this case our Purcell factor is:

$$C_\delta = \frac{\Gamma_\delta^{cav}}{\Gamma^{fs}} \tag{3.1}$$

for Γ_δ^{cav} the transition rate to a particular cavity mode. We will obtain the Purcell factor using Eqn.3.1 with spontaneous emission rates found using Fermi's Golden Rule. A general version of Fermi's Golden Rule can be written [44]:

$$\Gamma = \frac{2\pi}{\hbar^2}\int_0^\infty |H'|^2 \rho(\omega)\Lambda(\omega)d^3\omega \tag{3.2}$$

Here H' is the interaction Hamiltonian that couples electronic and photonic subspaces and $\rho(\Lambda)$ is the photonic(electronic) density of states, as a function of photon frequency ω . We can use Eqn.3.2 to find Γ_δ^{fs} or Γ_δ^{cav}, depending on which $\rho(\omega)$ is employed. Explicitly our interaction Hamiltonian will be given as:

$$H' = \sum_k \hbar(g_k \left|e\right\rangle \left\langle g\right| \hat{a} + g_k^* \left|g\right\rangle \left\langle e\right| \hat{a}^\dagger) \tag{3.3}$$

for $\left|e\right\rangle$ ($\left|g\right\rangle$) the electronic excited(ground) state, $\hat{a}^\dagger(\hat{a})$ the photonic mode raising(lowering) operator and

$$g_k = \frac{\mu \cdot \mathbf{E_k}}{\hbar} \tag{3.4}$$

the single photon coupling rate defined by the interaction of our dipole operator μ and the photonic electric field $\mathbf{E_k}$ representing the photonic mode with $\mathbf{k} = \omega/c\hat{k}$. We assume a perfect two level system with transition frequency ω_e such that:

$$\Lambda(\omega) = \delta(\omega_e - \omega). \tag{3.5}$$

Then to first derive the free space emission, one can write density of states as[45]:

$$\rho^{fs}(\mathbf{k})d^3\mathbf{k} = \frac{\mathbf{k}^2 d\mathbf{k} sin(\theta) d\theta d\phi V}{8\pi^3} \tag{3.6}$$

This can be used[45] to find:

$$\Gamma_\delta^{fs} = \frac{\omega_e^2 V}{3\pi c^3}|g|^2. \tag{3.7}$$

Here I have dropped the subscript on g as it now assumed to be that relating to the photonic mode that couples to the emitter transition. If instead we consider a cavity mode with decay rate κ and resonance frequence ω_c:

$$\rho^{cav}(\omega) = \frac{2}{\pi}\frac{\kappa}{4(\omega - \omega_c)^2 + \kappa^2} \tag{3.8}$$

and

$$\Gamma_\delta^{cav} = 4|g|^2\frac{\kappa}{4(\omega_e - \omega_c)^2 + \kappa^2}, \tag{3.9}$$

which upon resonance between the cavity and atomic transition can be used to calculate a commonly seen form of the Purcell factor:

$$C_\delta = \frac{4|g|^2}{\kappa\Gamma^{fs}}. \tag{3.10}$$

We can rewrite g in terms of the effective mode volume[38] using the single photon maximum field strength in the cavity $E_{max} = \sqrt{\frac{\hbar\omega}{2\varepsilon_0 n^2 V}}$ and $\eta = \frac{\mu\cdot E}{|\mu|E_{max}}$, were η is evaluated at the position of the emitter. Exercising $g(V)$ in Eqn.3.10:

$$C_\delta = \frac{3Q}{4\pi^2 V}\left(\frac{\lambda}{n}\right)^3 \frac{\kappa^2}{4(\omega_e-\omega_c)^2+\kappa^2}\eta^2, \tag{3.11}$$

which says the Purcell factor is maximal when the electronic system is on resonance with the cavity, positioned at an anti-node and aligned with E. Here we explicitly see that this ideal case is only a function of cavity parameters.

3.2 Deviation from the ideal case

In reality, the emission spectra of defect centers are far from Dirac functions. A couple consequences of this will be briefly explored in this section. The first effect I will discuss arises from existence of the phonon sideband, which significantly reduces the transition strength of coherent photons coming from the NV ZPL. By opening our discussion to the phonon sideband we remove the purely two-level nature of the NV and will need to distinguish between the decay rate of the NV as a whole, Γ_{nv}, and that which only emits into the zero phonon line Γ_{zpl}. With this we can now define the Purcell factor and ZPL Purcell factor. The Purcell factor is given:

$$C = \frac{\Gamma^{cav}_{zpl}}{\Gamma^{fs}_{nv}}. \tag{3.12}$$

This is a relevant figure of merit for the cavity-emitter system, to compare the enhancement of the ZPL transition with respect to free space decay to all radiative channels. In contrast, the ZPL Purcell factor takes form:

$$C_{zpl} = \frac{\Gamma^{cav}_{zpl}}{\Gamma^{fs}_{zpl}}. \tag{3.13}$$

This value tells us only the enhancement of the zero-phonon-line transition. This is equivalent to imagining that the ZPL is a two level system, but may differ from C_δ because it may consider finite line widths.

All defect centers have finite linewidths as a result of population decay and dephasing processes, which in solid-state systems are often a result of phonon interactions[46]. This will be the second effect discussed in this chapter. In particular, we will consider a form of C that is important for broad emitters.

Due to the temperature-dependent Jahn-Teller effect the NV ZPL is broad at room temperature[47, 48], but narrow at cold temperatures where it can often be considered a Dirac function with respect to the cavity linewidth. Only for these cold-temperature narrow linewidths can we expect Purcell enhancement. That said, while Purcell enhancement is our goal, this thesis will explore characterization of diamond microdisks by using *the PSB at room temperature*. Therefore the generalization of C for broad emitters is to gain an appreciation and understanding of the regime in which measurements of this thesis were actually taken.

3.2.1 Franck Condon Effect

As habitants of the diamond lattice, defect centers are prone to phonon interactions, which cause the large PSB in Fig.3.1(a). The PSB is a consequence of electronic state dependence on lattice vibrations, with the most basic (Huang-Rhys) model treating vibronic levels as a single, quantized harmonic oscillator dependent on nuclear displacement[49],Fig.3.1(b). The Franck-Condon principle says that transition amplitudes between ground and excited states are proportional to the relevant matrix element of the dipole operator[50]. Essentially, this amounts to transitions being proprotional to the ground and excited state wavefunction overlap[51]. Non-radiative decay to lower vibronic levels is fast so we generally assume that the intial state $|i\rangle$ is in the lowest vibronic sublevel (n=0) of the excited state. It can then decay to a final state, $|f\rangle$, which is one of several

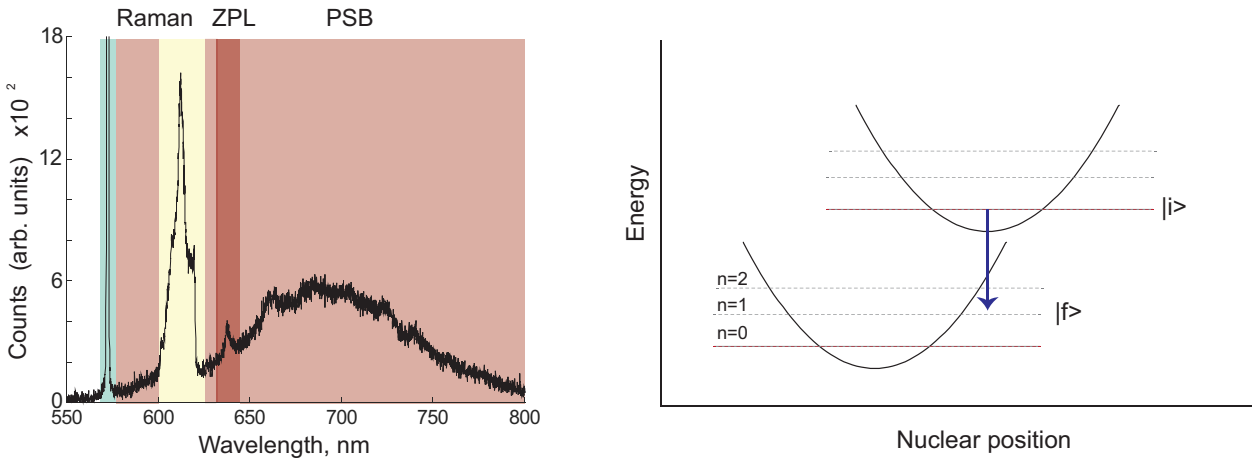

Figure 3.1: (a) A typical photoluminescence spectrum from diamond, showing the ZPL (shaded dark red) and phononsideband (stokes transitions of PSB shaded light red), as well as first (shaded green) and second (shaded yellow) order Raman lines. (b) Diagram of the Huang Rhys model. The lower harmonic oscillator represents the ground state and the upper shifted parabola, the excited state. Vibronic levels are given in dashed lines, with n photons. An example PSB transition is given by the blue arrow.

ground state sublevels with n phonons (Fig.3.1(b)). We can find that[51]:

$$|\langle f|\hat{\mu}|i\rangle|^2 = \mu_\delta^2 e^{-S}\frac{S^n}{n!} \tag{3.14}$$

where S is the Huang-Rhys parameter describing the strength of coupling to the nuclear positions and μ_δ is the transition dipole moment matrix element assuming a two level system. If $S < 1$ then the largest overlap is at the $n = 0$ transition, but for the NV $S \sim 3.6$[51], and contributions from higher vibronic levels are very important. Fast decay rates of these higher vibronic states[52] give them very broad linewidths, causing several of the transitions to spectrally overlap and result in the shape we see in Fig.3.1(a). Since the sidebands are not resolved from one another we often refer to one "phonon sideband" though it can be well represented by a superposition of *seven*[52].

Though dephasing effects can be mitigated by moving to low temperatures, the same is not true for the PSB. The majority of the PSB is red-shifted, meaning that the NV center has *lost* a phonon. Regardless of temperature an excited NV center may always *add* energy to the lattice, though the probability of it obtaining one (having blue-shifted PSB) relies on temperature-dependent phonon occupation.

Sometimes in literature the Debye Waller factor, $\zeta \sim e^{-S}$, is mentioned in place of the Huang Rhys Paramter. This represents the percent emission into the ZPL, as a fraction of total NV emission - for $S = 3.6$, $\zeta \sim 0.03$. From this we can now appreciate the sepration of our Purcell factor defintions. Since $g \propto \mu \cdot E$, by Eqn.3.14 our g_{zpl} must be scaled from the case that assumes the NV is a two level system with g_δ. We can think of this as:

$$\begin{aligned} C &= \frac{4g_{zpl}^2}{\Gamma_{nv}^{fs}} \\ &= \frac{4\zeta g_\delta^2}{\Gamma_{nv}^{fs}} \end{aligned} \tag{3.15}$$

Similarily, since C_{zpl} is a quantity that assumes the ZPL to be a two level system, we can see with some simple manipulation that:

$$\begin{aligned} C &= \frac{4g_{zpl}^2}{\kappa\Gamma_{zpl}^{fs}} \frac{\Gamma_{zpl}^{fs}}{\Gamma_{nv}^{fs}} \\ &= \eta_{dw} \times C_{zpl} \end{aligned} \tag{3.16}$$

This makes clear how η_{dw} greatly affects the NV center's potential to generate coherent photons. I would also like to note that while the SiV has a much higher Debye Waller factor than the NV, it seems to suffer from a poor quantum efficiency. Having not studied this in enough detail I refrain from further discussion here, though one could turn to the Supplementary Information in Ref[53] for an example.

3.2.2 Broad emitters and the Master Equation

In Chapter 5, the PSB will be used for device characterization. To understand the regime in which this characterization is performed, this section will address key points of a master equation model that includes broad emitters - though it can also be used to reproduce the ideal results. Note that while work has also been done to integrate the Franck Condon effect into a master equation approach (e.g.,[54]), this is not addressed here. In the following I summarize results of Ref[52] which are largely an extension from the works in ref[55, 56]. Transition levels are summarized in Fig.3.2 where we keep ω_c as the cavity frequency and ω_e as the transition frequency for the ZPL,

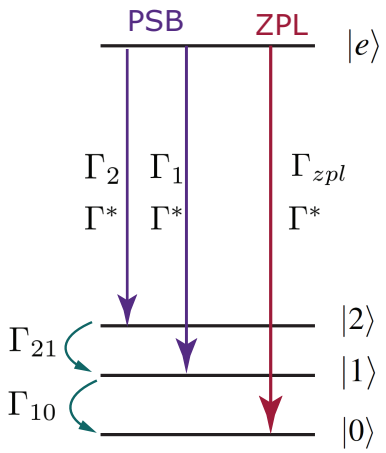

Figure 3.2: Decay rates relevant to the broadband model. Γ^* is pure dephasing, Γ_{zpl} and Γ_i are spontaneous emission rates of the relevant transition, $\Gamma_{i,i-1}$ are phonon decay between the vibronic sublevels i and $i-1$.

as before. We add transitions from $|e\rangle$ to the i^{th} vibronic level of the ground state with spontaneous decay Γ_i and energy $\hbar\omega_i$ (i.e., $\omega_0 = 0$). The Hamiltonian for the full NV-cavity system is:

$$\mathscr{H} = \hbar\omega_e\sigma_{ee} + \hbar\omega_c a^\dagger a + i\hbar g_{zpl}(a^\dagger\sigma_{0e} - \sigma_{0e}^\dagger a) + \sum_{i=1}^{N}\left(\hbar\omega_i\sigma_{ii} + i\hbar g_i(a^\dagger\sigma_{ie} - \sigma_{ie}^\dagger a)\right) \tag{3.17}$$

Here I take the convention $\sigma_{ij} = |i\rangle\langle j|$. This Hamiltonian so far neglects decoherence and dephasing. In a master equation approach, losses are introduced through operators, using the Lindblad superoperator $\mathscr{L}$ and density matrix $\hat{\rho}$. For the current problem, these are identified by [52] to be:

$$\begin{aligned}
\mathscr{L}_{damp}^{cav} &= \kappa\mathscr{L}[\hat{a},\hat{\rho}] \\
\mathscr{L}_{damp}^{at} &= \Gamma_{zpl}\mathscr{L}[\sigma_{0e},\hat{\rho}] + \sum_{i=1}^{N}\Gamma_i\mathscr{L}[\sigma_{ie},\hat{\rho}] \\
\mathscr{L}_{g.s.-relax}^{at} &= \sum_{i=1}^{N}\Gamma_{i,i-1}\mathscr{L}[\sigma_{i,i-1},\hat{\rho}] \\
\mathscr{L}_{deph}^{at} &= -\frac{\Gamma^*}{2}\begin{pmatrix} 0 & \rho_{12} & \dots & \rho_{1N} \\ \rho_{21} & 0 & & \\ \vdots & & 0 & \\ \rho_{N1} & & & 0 \end{pmatrix}
\end{aligned} \tag{3.18}$$

Respectively these operators represent the cavity damping, emitter damping, lifetime broadening via ground state relaxation, and emitter dephasing. The master equation itself uses these operators

and is defined:

$$\dot{\hat{\rho}} = \frac{i}{\hbar}[\hat{\rho}, \mathscr{H}] + \mathscr{L}^{cav}_{damp} + \mathscr{L}^{at}_{damp} + \mathscr{L}^{at}_{relax} + \mathscr{L}^{at}_{deph}. \tag{3.19}$$

It allows us to solve for dynamics of a system, noting that:

$$\frac{d}{dt}\langle \hat{A} \rangle = tr(\dot{\hat{\rho}}\hat{A}). \tag{3.20}$$

A good discussion of the master equation and its basics can be found in [57]. The main results of the derivation from [52] are the dynamics of the cavity photon number population $\langle a^\dagger a \rangle$ and electronic excited state population $\langle \sigma_{ee} \rangle$:

$$\begin{aligned} \frac{d}{dt}\langle a^\dagger a \rangle &= -(\kappa + \Gamma^{cav}_{zpl})\langle a^\dagger a \rangle + (\Gamma^{cav}_{zpl} + \sum_i \Gamma^{cav}_i)\langle \sigma_{ee} \rangle \\ \frac{d}{dt}\langle \sigma_{ee} \rangle &= -(\Gamma + \Gamma^{cav}_{zpl} + \sum_i \Gamma^{cav}_i)\langle \sigma_{ee} \rangle + \Gamma^{cav}_{zpl}\langle a^\dagger a \rangle \end{aligned} \tag{3.21}$$

The coefficient of $\langle \sigma_{ee} \rangle$ in Eqn.3.21 tells us the total decay rate of our excited state. The decay rates in Eqn.3.21 are given by:

$$\begin{aligned} \Gamma^{cav}_{zpl} &= \frac{4g^2_{zpl}}{\kappa + \Gamma + \Gamma^*}\Theta_{zpl} \\ \Gamma^{cav}_i &= \frac{4g^2_i}{\kappa + \Gamma + \Gamma_{i,i-1} + \Gamma^*}\Theta_i. \end{aligned} \tag{3.22}$$

Γ^{cav}_{zpl} is still the transition rate from the ZPL into the cavity mode. However, now there are transition rates Γ^{cav}_i into the cavity from the i^{th} PSB transitons. They are detuned from the cavity resonance by $\delta_i = \omega_c - \omega_i$, which affects the emission rates through the parameters:

$$\begin{aligned} \Theta_{zpl} &= \frac{1}{1 + \left(\frac{2\delta_{zpl}}{\kappa + \Gamma + \Gamma^*}\right)^2} \\ \Theta_i &= \frac{1}{1 + \left(\frac{2\delta_i}{\kappa + \Gamma + \Gamma_{i,i-1} + \Gamma^*}\right)^2}. \end{aligned} \tag{3.23}$$

Our total radiative decay is $\Gamma = \Gamma_{zpl} + \sum_{i=1}^{N} \Gamma_i$.

Eqn.3.22 reduces to its common form if we assume $\kappa \gg \Gamma, \Gamma^*, \delta_i$, i.e. that the ZPL has a narrow linewidth as it does at cold temperatures and that it is positioned within the cavity linewidth. However, in the regime relevant to measurements in this thesis $\Gamma^* \gg \kappa$ and the PSB shows even

further broadening from $\Gamma_{i,i-1}$. This results in emitter properties limiting the system, in place of the cavity. It follows that C_{zpl} can take the form of C_δ by replacing Q with Q_{em} in Eqn.3.11. The effect can be alternatively thought of as[52] scaling our C_δ by the ratio of the cavity emission that overlaps with the broadband emitter spectrum, i.e. by $\kappa/(\Gamma_i + \Gamma^*)$. Furthermore we can now define $C_{PSB,i} = \Gamma_i^{cav}/\Gamma_{nv}^{fs}$ for the i^{th} PSB. Since we will use the PSB for characterization, it is these $C_{PSB,i}$ that will be relevant. What will be key for the subsequent analysis is that $C_{PSB,i}$ is $\ll 1$ and, importantly, does not depend at all on the cavity Q.

As a final note, the presence of Γ in the effective decay rate represents emission outside the cavity, which is ~ 0 for a closed cavity system but $\sim \Gamma_{fs}$ for an open system [58]. We did not see this factor when using Fermi's Golden Rule because we considered only the relevant cavity transition.

Chapter 4

Measurement Technique

In this section I will explain in detail the setup shown in Fig.4.1, which merges free-space optics and visible-wavelength fiber-taper probe measurements. This setup was designed to enable three key measurement techniques: confocal microscopy, fiber taper transmission, and fiber-taper-collected PL. Fig.4.1 shows that the free space optics are aligned atop a raised breadboard while the sample and fiber taper probe are mounted on the optical table, and housed inside a nitrogen purge box to prevent degredation. Carefully designed brackets (Label "D" in Fig.4.1(a)&(c)) can focus a free space optical path through the objective lens onto a device that is simultaneously coupled to the fiber taper (Fig.4.1(c)).

In this chapter I will first discuss the challenge of integrating the free-space and fiber-taper setups. Next, I will divide explanation of the setup according to the measurement technique of interest. In particular for the fiber-taper PL measurement, I will explain its importance to this thesis. Lastly, I will review some key points of the brackets designed which are critical for the setup merge. Parts are largely summarized in Appendix A, if not in text.

4.1 A note on integration

The challenge in integrating these capabilities is perhaps subtle. However, a large source of complication for this merge is the nitrogen purge box. This purge box is absolutely necessary to maintain the quality of our fiber tapers. Dust and contaminants from the air can land on the taper and lower transmission, and air currents from regular movements can completely break it. Creating the purge box itself is not an issue, however, as an interface where all the components meet, it is critical.

In particular, we need an adjustable bracket that will allow objective lenses of varying focal length to focus on the sample, without hitting the top of the box. These lenses, also of varying

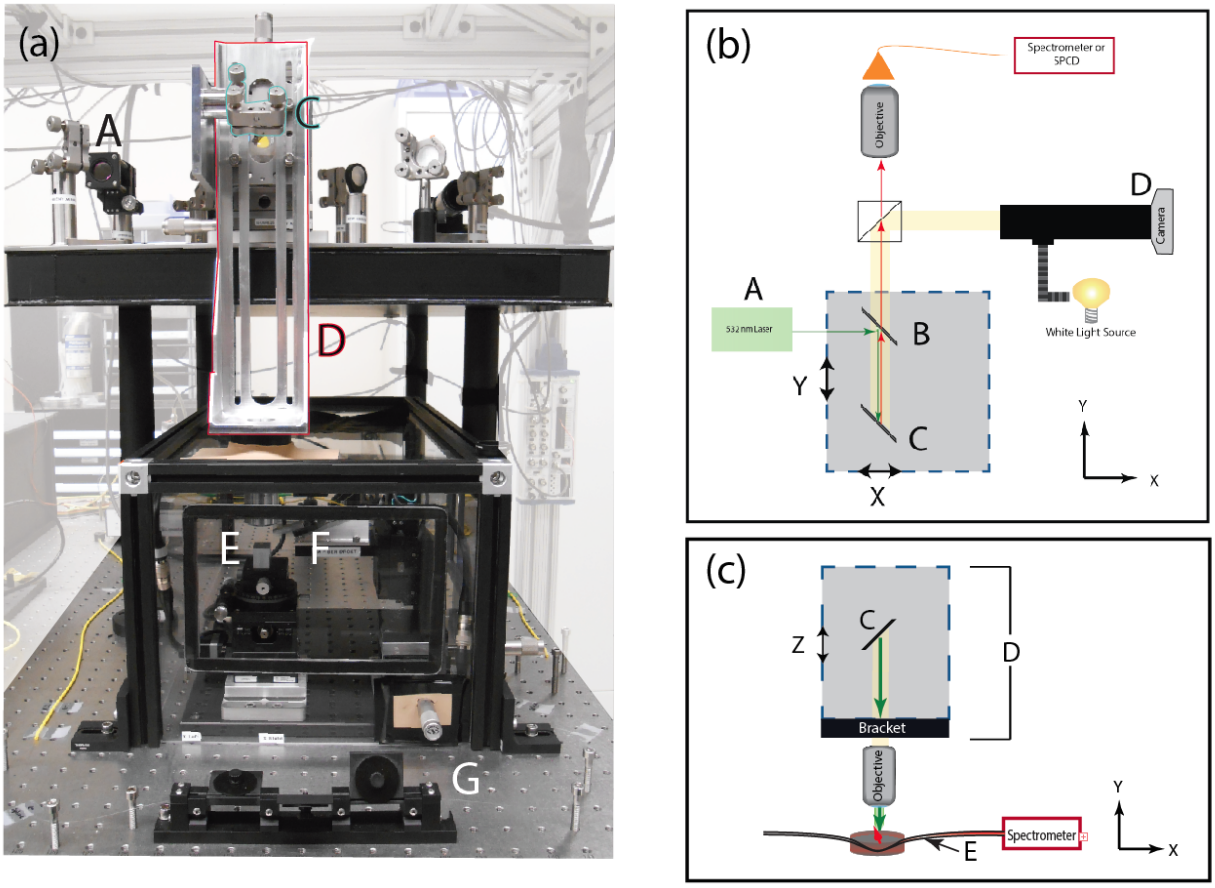

Figure 4.1: (a) The merged free-space and visible-fiber-taper setup. Components on the raised breadboard are shown in a simplified schematic in (b). The breadbhoard holds the optics for while light illumination, green laser excitation and confocal collection. Mirror B is a dichroic. (c) shows the optical pathway connecting free-space optics to the sample, which can be simultaneously coupled to the fiber-taper probe.

thickness, must fit through a hole in the box lid and be given some XY translation range to provide freedom for the imaging position. Of course, the edges of this hole must be covered to keep the box environment clean. The fiber taper must have significant translation range around the taper, and must be on a holder that will not conflict with either the objective lens or the sample holder. Additionally, the box requires holes to accommodate access to both translation stage micrometers for the fiber. It cannot be placed arbitrarily because, as a result of integrating the free space paths, we face positioning constraints based upon the alignment of optics on the raised breadboard. The setup described below meets these requirements.

4.2 Confocal & free space setup

The purpose behind confocal microscopy is to obtain *point* excitation and collection whose paths are overlain[59]. In the context of color centers, it can be used to obtain a spatially selective signal, potentially from a single emitter. This signal can be detected as a photon count number or as a spectrum. Very basic measurements include using spectra to identify color centers and using photon counts to image single emitters.

In the current example, NV centers are excited off-resonantly with a 532nm CW laser as shown in Fig.4.1. The green laser has energy higher than the NV ZPL transition and therefore ensures excitation of the NVs, which can then emit anywhere in the PSB (roughly 600-800nm). NV emission subsequently retraces the green laser path, until a dichroic mirror. At the dichroic, the red light passes though where green light should be reflected. Note that this sensitive retracing of the red laser along the green path is dependent upon the green laser entering the objective lens straight and on-axis.

Traditionally, the collection path is then focused onto a pin hole before the signal is sent to a detector - either single photon counters or the spectrometer. This pinhole is the key feature because it eliminates the majority of signal coming from outside the focal point, thereby establishing the point collection. In our case the collection beam is fiber coupled and the fiber core is implented

to replace the pin hole. Before focusing the collection signal into the fiber, there is a 550nm long pass filter to remove reflected excitation light that will inevitably pass through the dichroic. Additionally, because we are illuminating bulk diamond in addition to the NVs, there will be a large contribution from the first and second order Raman signals at $\sim$ 572nm and $\sim$ 610nm. These should be removed during alignment with the APDs using, e.g., a 650nm long pass.

4.2.1 Green laser excitation

A green laser is coupled to this setup through fiber optics, from an autonomous setup with output-coupling optics that are not discussed here. The fiber output coupler is housed in a cage system and the beam is collimated using an aspheric lens. Fixed optical posts should place the green laser at the beam height of the system ($\sim$ 102mm). To compensate for any angular adjustments, an extra mirror (not shown in Fig.4.1(b)) is used. Finally, a 532nm bandpass filter in front of the green laser cleans the signal.

4.2.2 Collection

Emission from the NVs will be collected by a cone defined by the objective lens NA[1]. Though possible to switch the objective, it should always be infinity-corrected[2]. Additional mirrors (omitted from Fig.4.1(b)) after the beam splitter provide the degrees of freedom for adjusting the collection path. A second objective lens housed in a z-axis (optical-axis) translation stage is coupled to a fiber in an XY kinematic mount, both locked onto the same optical cage. While the mirrors provide positioning of the collection beam on the aperature of the objective lens, the XY kinematic mount provides positioning of the fiber chuck with respect to the objective lens focus. The z-axis allows for focusing of the collection path onto the fiber chuck. Note that the NA of the fiber must be greater than that of the objective lens to ensure the full signal will be collected. When performing

[1] If only performing confocal measurements the NA=0.8, 100X lens is suggested, however, if using the angled fiber mount, the short focal length may cause it to hit the mount. If a fiber taper is mounted it is safer to use the Mitutoyo 50X, NA=0.55

[2] An infinity corrected lens means the back focal length is very long, such that the output is very close to a collimated beam.

confocal measurements it is best to put the beam splitter down for improved collection.

4.2.3 White light imaging

The white light path is used in all three setup configurations for device imaging. It makes use of separate positioning mirrors after the beam splitter in Fig.4.1(b), though for simplicity these mirrors are not included in the schematic. This path not only images white light, but the reflection of the green laser off the sample, which can be used for the laser alignment. In addition, it can be used to back-align the collection path. In this case, a red laser is connected to the collection path in place of single photon counters. It follows the path that NV emission should follow, but in the reverse direction. This allows the laser to be incident on the sample and reflect off the surface for imaging on the white light path CCD. This back-alignment is a critical tool for off-axis confocal collection, briefly discussed in Section 4.4.1, and the reason for including a beam splitter here, rather than a mirror.

4.2.4 Outlook

At present, basic confocal collection can be performed and general substrate measurements taken. However, proper functioning of the confocal path for this setup is limited due to a lack of fine positioning control, especially in the vertical direction. It was built to include the option for such control, with the addition of piezo stages. The purpose then for having such a system at room temperature would be for quick characterization of samples to identify presence of NV or SiVs in samples. It is also secondary check to the fiber-PL capability, which cannot be used on the bulk. Overall, the confocal arm here can reroute some of the traffic on our cryostat setup, for characterization measurements that do not require low temperatures. Also note that while not yet tested, the setup has been designed for the potential to integrate our EMCCD. In particular, spacing of the white light optics has been done carefully to ensure room for this large and heavy camera to be secured on the optical breadboard. Posts and spacers for this purpose have been ordered to place the sensor at the optical beam height.

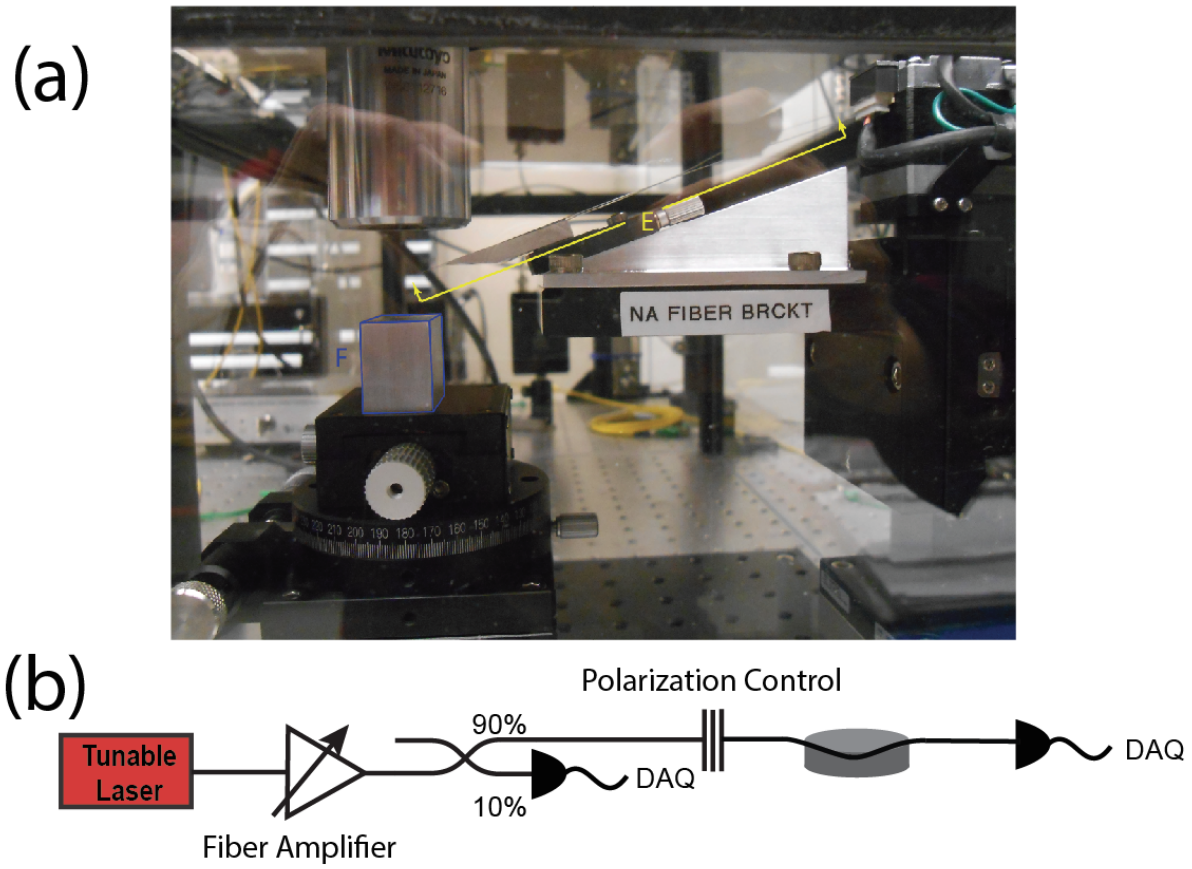

Figure 4.2: (a)Fiber taper setup. The sample mount (outlined blue, "F") will hold a sample chip and sits atop a goniometer for fiber-sample tilt adjustment, as well as motorized stages. It can be imaged by the objective above and coupled to via the fiber taper, which is mounted along the outlined line (yellow, "E"). It has manual XY translation and motorized Z translation. (b) Fiber taper schematic. A tunable laser signal can be attenuated with a fiber attenuator. A 10% tap off is taken to remove wavelength-dependent laser features from the signal, post-processing. Polarization control before the device allows coupling to both TE and TM modes.

4.3 Fiber taper transmission

As largely discussed in the background section, optical transmission measurements can be performed using a fiber taper probe. These measurements allow us to characterize the optical resonances of our devices.

A close up of the fiber-sample interface is highlighted in Fig.4.2(a) while a schematic of the setup is given in Fib.4.2(b). The fiber tapers for this setup were made ("pulled") to be single mode at $\sim$ 640nm. Visible fiber tapers are even more delicate than their telecom counterparts since their

waist must be so thin - in this case the ideal diameter is approximately $\sim$ 500nm. Note that due to the fabrication method, our microdisks are at the same height as the substrate (Fig.2.1). In order to couple selectively to devices without touching the substrate, we "dimple"[60] the fiber so it has a shape similar to that shown diagramatically in Fig.4.2.

Rough fiber taper positioning is accomplished with manual XY stages. These are usually only used when a new fiber has been mounted in the setup. Otherwise the taper is left in place and taper-device positioning is controlled by the sample XY control. The sample XY and fiber Z translation are accomplished with 50nm resolution stepper-motor translation stages (Suruga Seiki), controlled via a LabView program. At the microscale it is common that neither the sample nor fiber will be exactly straight (i.e. not exactly parallel to the optical table surface). If the fiber is angled with respect to the sample then the dimple will not be the lowest point on the fiber as it is lowered. This will cause the fiber arm to contact the substrate, which is not desired. To compensate for this we adjust the relative fiber-sample angle using a manual goniometer underneath the sample holder.

With respect to positioning the fiber for a measurement, I note that as in ref[27], suspected coloumb interactions when the taper and microdisk are in close proximity attract the taper so it touches the microdisk surface. However, if the fiber is favourably dimpled, it is possible to limit, if not remove, this contact by taking advantage of the window-substrate geometry. While maintaining a sample surface - taper distance to prevent attraction, the taper can be roughly positioned along the sample plane. Then, by lowering the taper quickly, substrate contact with the fiber on either side of the taper holds the position firmly enough to avoid being pulled to the edge of the microdisk. Though the taper-disk distance has not been quantified, PL mesaurements comparing cases of the taper blatantly touching the microdisk against those with strategic taper-substrate contact (Fig.4.3(b)), show a strong improvement in the loaded Q factor, indicating that this contact has been lowered, if not removed.

To perform a transmission measurement we use input from a tunable laser, which is controlled via computer program[3]. Wavelength data from the laser controller can be directly connected to a

[3]Coded in-house thanks to David Lake

DAQ board via BNC, and is needed to monitor our signal. The optical laser signal is connected via fiber optics to a fiber attenuator, allowing some manual control of the input power[4]. Wavelength- and time-dependent fluctuations of the laser input make it difficult to discern low-resonance contrast modes from variations in the laser signal. To mitigate this effect, a $\sim 10\%$ tap-off of the laser measures features of the laser input to the fiber taper, providing a means to divide-out laser features from the transmitted signal and aiding identification of microdisk resonances. The remaining $\sim 90\%$ laser input is then sent into a polarization controlling paddle unit that mimicks a 1/4-1/2-1/4 λ-plate configuration. As in free-space optics where a birefringent waveplate has a slow and fast axis, stress-induced birefringence[61] creates a slow and fast axis in the paddle controller, based upon the number of loops in each paddle. By rotating the axes of these three plates, one should in principle be able to access any output polarization for any arbitrary input polarization. As discussed in the background, the taper then couples to a device and the transmitted signal is collected with a photodetector. Photodetectors used for both the 90% and 10% taps are then also connected to the DAQ board, allowing us to monitor the signals in real-time and perform the post processing. The final result of these measurements give features like, e.g. Fig.2.3, where one should note that the data here has been fit such that the signal on either side of the transmission dips is enforced to a value of T=1.

4.4 Fiber-collected PL

Unlike at telecom, where laser range spans 100s of nanometers, visible wavelength transmission measurements are limited to $\sim$ 5nm near 637nm and 737nm - the nitrogen (NV) and silicon vacancy (SiV) transitions. This narrow window makes mode identification difficult because we cannot, as mentioned before, measure more than one FSR. However, to surmount this problem we can make use of the fact that optical grade SCD chips have a high density of instrinsic nitrogen

[4]These visible diode lasers operate best near maximum current. At lower currents they are more suceptible to mode-hops and at even lower currents they will begin to diode rather than lase. Thus, power adjustment via the laser controller is not ideal.

vacancy centers, which emit over a visible range of roughly 200 nm. By exciting the NVs through free-space optics and collecting their emission with the fiber taper it is possible to study microdisk modes over a longer wavelength range. A schematic of this setup is giving in Fig.4.1(c).

4.4.1 Advantage of fiber-taper collection

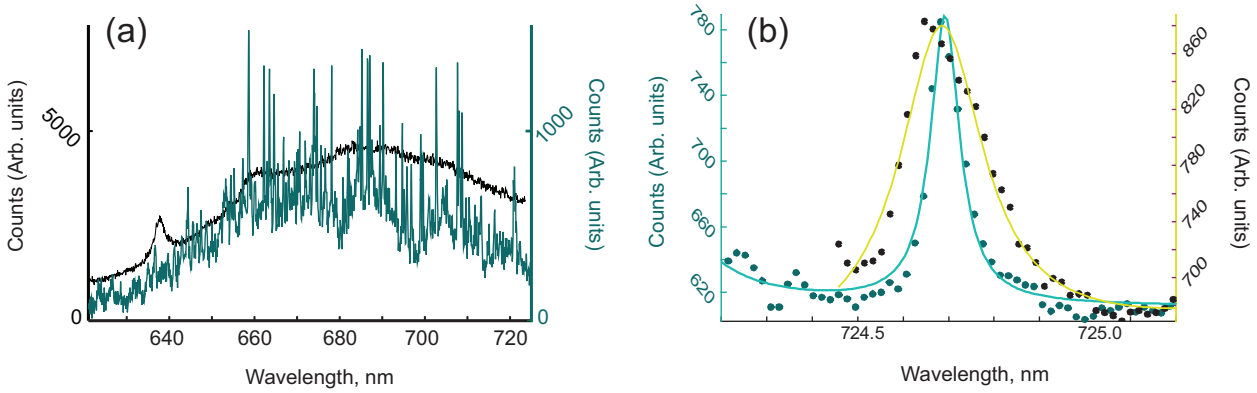

Figure 4.3: (a) PL measurements taken on the Cryostat setup, from an NV-implanted electronic grade diamond sample. Confocal PL scan of substrate NVs (black) and off-axis scan on a microdisk, showing modes (teal) (b) Taper touching the microdisk (yellow) and presumed not to be touching (teal)

It should be noted that defect center PL characterization through free space has been performed with other nanophotonic devices[34, 26, 30, 32, 33]. We initially attempted similar measurements on a previously exisiting free-space setup. The collection was first performed confocally, but was unfruitful presumably due the microdisk-coupled NV signal being masked by either substrate or uncoupled microdisk NVs. We then attempted an off-axis configuration where, via back alignment using a red laser, the collection beam path was aligned μm from the excitation path while imaging both beams on a CCD camera. This off-axis positioning aims to collect less from uncoupled NVs and more from light circulating the microdisk. After many attempts the spectrum in Fig.4.3(a) was obtained. However, sensitivity of this method makes it very cumbersome, since one must switch between the alignment laser and the spectrometer for every adjustment. Furthermore, for testing different microdisk sizes, adjustment and optimization of this alignment for every microdisk would

be necessary.

Fiber taper collection, on the other hand, provides a method for selectively coupling to and assessing PL from microdisks. We are able adjust our coupling relatively easily by monitoring transmission measurements and, once placement is correct, we are then able to compare these transmission measurements to our PL data, providing more for analysis.

4.5 Mirror mount and objective holder

The microscope objective in this setup has manual XYZ translation stages. This freedom is extremely important for the setup, including imaging aid during goniometer (sample-to-fiber angle) alignment, and enabling green laser positioning while the fiber-taper is coupled to a microdisk. This requirement begs for a design that enables such positioning without destroying the carefully aligned excitation and collection paths. Other researchers have opted for galvomirrors to deal with this.

Fig.4.4 shows designs of the three custom pieces that allow our setup to accomplish this. Carefully designed, these pieces translate mirrors A and B with the objective lens. Note that A is our dichroic. So long as the system does not move out of range such that either of the green laser or collection beams incident on A become clipped, then all the optics outside this unit remain unchanged.

Note that while I created designs for these pieces to fit with the dimensions and needs of my setup, the base ingenuity must be attributed to Harishankar Jayakumar, whose original concept I mimicked from an existing setup in our lab.

The blue plane of the XYZ bracket in Fig.4.4(a) attaches to the X and Y stages in Fig.4.4(c), upon which the dichroic mirror (A) is positioned. A manual z-stage (green), with an optical aperature in it to allow laser and collection path access, is mounted on the red plane of the bracket. Mirror B in Fig.4.4(c) is then mounted on the bracket's yellow plane, to deflect signal down into the aperature C. Aperture C has female SM1 threads. These threads do not match any of our

objectives, but as a standard thread, are attachable via standard adapters.

The long apertures A and B in the objective-holder bracket are necessary for two reasons: (1) to provide us space to exchange objective lenses outside the purge box, without damaging our fiber or sample; (2) to adjust the relative height of the bracket to compensate for differing objective focal lengths. Note that for our shortest focal length objective lens an SM1 lens tube must be used to bring it close enough to the sample. The bracket could not be made longer to compensate for the short focal length due to restrictions on the box height (which is constrained by the height of pieces inside). Label "A" in Fig.4.4(b) is a set of through screw holes allowing the bracket to slide up and down and be secured at any point along the track, to the z-translation stage in Fig.4.4(c). Fig.4.4(b) "B" provides an aperature "track" that allows light to pass regardless of where the objective holder is secured.

Protruding threads (D) on the bracket in Fig.4.4(b) are used to attach an SM2 tube. This tube was carefully chosen to help close the hole made for the objective lens. In particular a piece of latex cut to fit the tube covers the open space in the lid, when the bracket is lowered. Without the tube, we would require a seal that works for various objective lens sizes. In this case, however, neither the tube nor latex piece need to be removed or replaced during objective lens changes.

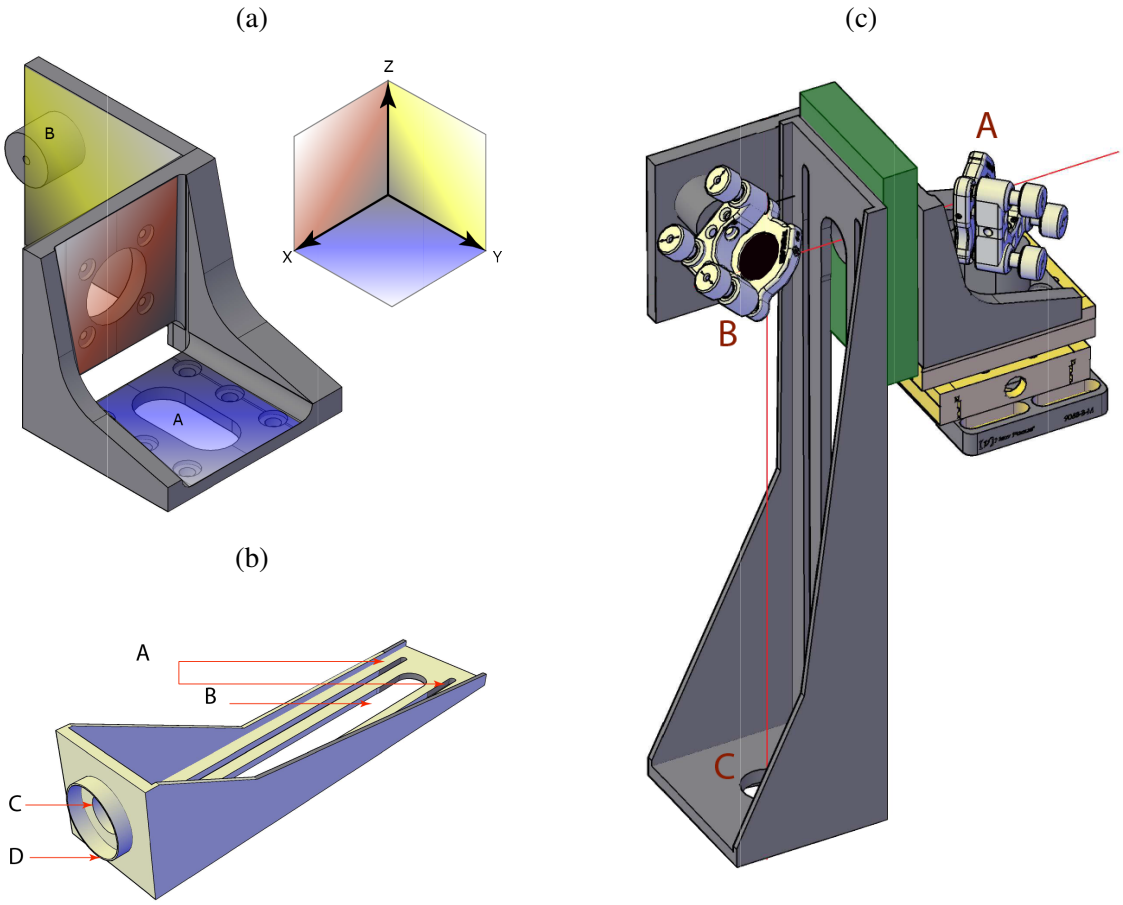

Figure 4.4: Custom-designed pieces. (a) XYZ bracket; (b) Objective-holder bracket; (c) The XYZ bracket rests upon regular XY stages and a Z stage with an aperature is ounded on it (green). The objective-holder bracket is then mounted on the stage for focusing purposes. Mirror A is our dichroic, mirror B deflects the signal to the objective.

Chapter 5

Microdisk characterization

In this chapter we use the system described in Chapter 4 to perform spectroscopy on diamond microdisks by simultaneously implementing free-space excitation and fiber-taper collection. The results and analysis in this section are being prepared in a journal manuscript.

T. Masuda, J.P. Hadden, D. Lake, M. Mitchell, and P.E. Barclay. *Fiber-taper collected photoluminescence characterization of diamond microdisks*. (In progress).

I have written the manuscript myself, as well as performed the measurements and simulations. However, along the way I recieved significant input and assitance from my peers. This includes help with ideas, editing, provision of various analysis scripts, and aid with various setups. The devices tested here were made by David Lake and Matthew Mitchell. Further detail on these contributions has been given in the preface.

5.1 Representation of cavity spectra in taper-collected PL

At room temperature where the NV pure dephasing rate, Γ^*, is much greater than the natural linewidth, Γ, atom-photon coupling, g, and cavity decay rate, κ, the cavity is expected to act as a spectral filter[55] on the PSB PL. We therefore consider the use of the NV PSB as a white light source for the study of microdisk mode spectra, collected via fiber-taper. In this section we will investigate the fiber taper-collected PL signal by comparing it with high-resolution microdisk transmission data.

As Fig. 5.1 demonstrates, peaks in the PL signal align with resonances in the transmission spectrum, indicating collection from microdisk modes. We model the microdisk-fiber taper collection system using an input-output formalism, considering the j^{th} microdisk mode with field amplitude a_j, total loss rate κ_j, and resonant frequency ω_j. The mode is excited at frequency ω by a source

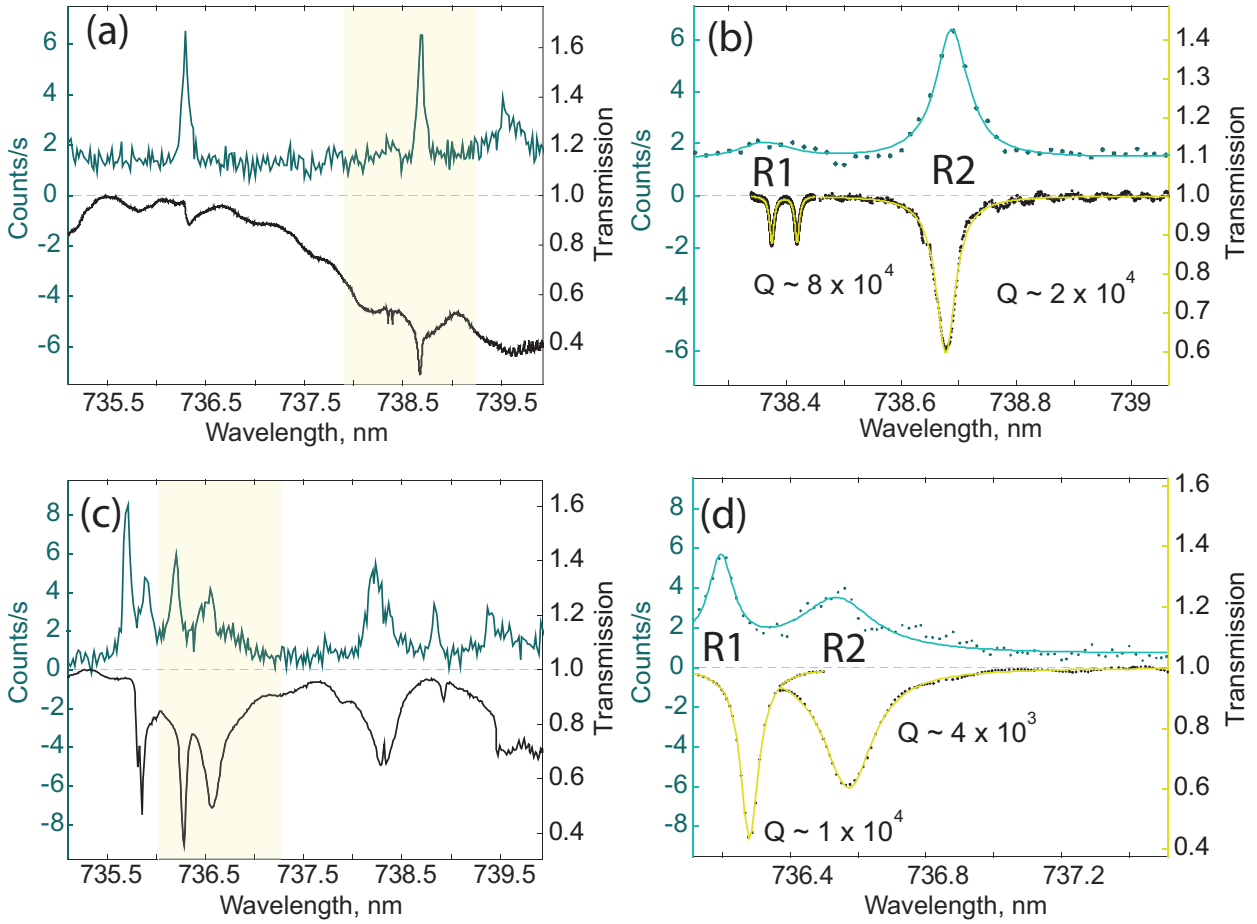

Figure 5.1: Transmission (black) and photoluminescence (teal) measurements for microdisk A (a,b) with [r,t]∼[2.0μm,800nm] and microdisk B(c,d) with [r,t]∼[3.1μm,850nm]. (a) and (c) show wideband data while (b) and (d) highlight resonances of interest and include fits used to extract quality factors. Broadening of the PL-measured cavity modes is attributed to spectrometer effects.

term s_j, here due to PL of the PSB. Given external coupling rate κ_j^e from the microdisk mode into the fiber taper and equation of motion:

$$\frac{da_j}{dt} = (i\Delta\omega_j - \frac{\kappa_j}{2})a_j + s_j, \tag{5.1}$$

where $\Delta\omega_j = \omega - \omega_j$, the collected PL intensity from mode j is $I_j = |\sqrt{\kappa_j^e}a_j|^2$. Using the steady state value of a_j evaluated from Eqn. 5.1:

$$I_j = \frac{\kappa_j^e |s_j|^2}{(\Delta\omega_j)^2 + (\kappa_j/2)^2}. \tag{5.2}$$

The measured PL spectra can be compared to the signal expected from Eqn. 5.2 using Qs extracted by fitting transmission data, where $Q_j = \omega_j/\kappa_j$. In particular, consider resonances $R1$ and $R2$ as

defined in Fig. 5.1 (b) and (d), for microdisk A and B respectively. Over the short wavelength ranges considered in Fig. 5.1, the PSB emission is taken to be locally flat, such that it is assumed microdisk modes within the same measured spectrum are equally excited, i.e. $s_{R1} = s_{R2}$. If in addition $\kappa^e_{R1} = \kappa^e_{R2}$ and both modes couple equally to the fiber taper, the intensity peak height $I_j(\omega_j) \propto Q_j^2/\omega_j^2$, can be used to select highest-Q modes. Under these conditions, the ratio of the peak height of resonance $R1$ to that of $R2$ would be:

$$\alpha^0 = \left(\frac{\omega_{R2} Q_{R1}}{\omega_{R1} Q_{R2}}\right)^2, \tag{5.3}$$

such that $I_{R1}(\omega_{R1}) = \alpha^0 I_{R2}(\omega_{R2})$. Table 5.1 summarizes the expected α^0. Comparison of α^0 to the measured PL data in Fig. 5.1 immediately indicates that PL peak heights cannot be used here to identify the highest-Q modes. This is most well demonstrated by considering the doublet $R1$ from microdisk A, which is barely discernable above the noise floor. α^0 suggests that $R1$ should have $22\times$ the intensity of the singlet $R2$, however $R2$ has a larger measured PL signal.

Disk	α^0	α^f
A	22	1.4
B	7.6	4.2

Table 5.1: Comparison of peak height intensity ratios α^0 and α^f for modes in Fig.5.1. For the doublet, the fitted Q^e_j is replaced by $0.5Q^e_j$ to compensate for uni-directional fiber taper collection.

If we now consider the external coupling to the fiber by allowing $\kappa^e_{R1} \neq \kappa^e_{R2}$ and taking Q^e_j as extracted from transmission data, the peak height ratio may be written:

$$\alpha^f = \frac{Q^e_{R2}}{Q^e_{R1}} \alpha^0. \tag{5.4}$$

Note that here, $s_{R1} = s_{R2}$ is still assumed. A comparison of α^0 to α^f in Table 5.1 shows that the predicted relative peak heights change based on the external coupling, leading to an order of magnitude change in the peak height ratio expected for $R1$ and $R2$ of microdisk A. Thus, spectral filtering by the fiber taper appears to play a key role in preventing the aforementioned Q assignment based on peak height. This may be attributed to the fact that stronger microdisk-fiber taper coupling, determined by the ratio Q^e/Q_j[43], can overcome a lower Q_j.

Despite considering the fiber-taper spectral filtering, α^f fails to fully explain the spectrum of microdisk A since $\alpha^f > 1$ and therefore shows at least an order of magnitude discrepancy from the measured PL where $I_{R1}(\omega_{R1}) < I_{R2}(\omega_{R2})$. This suggests that $s_{R1} \neq s_{R2}$ is possible - i.e., the modes are not being equally excited by PSB PL.

Excitation of the modes is dependent upon emission from an ensemble of NVs. The i^{th} PSB of each NV has a resonant frequency $\omega_{PSB,i}$, transition strength ζ_i, and cavity-influenced emission rate $\Gamma^j_{PSB,i} = C^j_{PSB,i}\Gamma^{fs}$. Here the $C^j_{PSB,i}$ represent generalized, "bad-emitter" Purcell factors [56], rewritten in terms of Q and V and based upon derived emission rates[52] of each PSB transition:

$$C^j_{PSB,i} = \frac{3}{4\pi^2}\frac{\zeta_i Q_{PSB,i}}{V_j}\left(\frac{\mu \cdot E_j}{|\mu|E_j^{max}}\right)^2 \frac{(\Gamma^j_{PSB,i})^2}{4(\delta\omega_{ij})^2 + (\Gamma^j_{PSB,i})^2}, \tag{5.5}$$

with μ the NV transition dipole moment, E_j the electric field of mode j and $\delta\omega_{ij} = \omega_{PSB,i} - \omega_j$. The purpose of these generalized Purcell factors is to demonstrate how cavity and emitter properties influence the emission into each mode. For intuition, this can be compared to the ideal case, where there is only one transition (i.e., no need to specify i) and $\kappa_j \gg \Gamma^j \gg \Gamma^*$:

$$C^j = \frac{3}{4\pi^2}\frac{Q_j}{V_j}\left(\frac{\mu \cdot E_j}{|\mu|E_j^{max}}\right)^2 \frac{\kappa_j^2}{4(\delta\omega_j)^2 + \kappa_j^2}. \tag{5.6}$$

We can interpret Eqn. 5.5 as scaling Eqn. 5.6 by ζ_i to take into account that only a fraction of NV emission goes into the i^{th} PSB. Furthermore the substitutions $Q_j \to Q_{PSB,i}$ and $\kappa_j \to \Gamma^j_{PSB,i}$ result from the fact that, unlike ideal case where our emitter acts like a dirac function with respect to a broad cavity linewidth, here our microdisk cavity modes take the role of a dirac function with respect to the broad PSB linewidths.

The discrepancy between measured PL ratios and those predicted by α^f may therefore be due to more efficient excitation of a particular mode, for example as a consequence of more NVs coupling to it, or better positioning and alignment of NVs with respect to E_j. In addition, as demonstrated by Albrecht *et al*[52], it is possible for NV emission to show effects beyond spectral filtering, which are not explained by Purcell enhancement. In summary, relative peak intensities are not representative of the resonance Q, even if fiber-taper coupling is taken into consideration via

Q_j^e. While the fiber-taper collected PL signal can be used to identify lower-Q resonance positions, poor collection of high-Q modes may prevent identification of the most interesting resonances in the PL spectra.

5.2 Phonon sideband range measurements

To better understand the fiber-taper microdisk system we next investigate which mode families demonstrate a strong PL signal. Families are classified by TE(TM)$_{p,q}$, for transverse electric(magnetic) polarization and WGM radial(vertical) order number $p(q)$. The free spectral range (FSR) between members of the same family, differing only by azimuthal number m, can be very roughly estimated for these microdisks using the refractive index of diamond n_d and the back-of-the-envelope calculation Eqn. 2.12 which suggests that the microdisks here should have FSR in the range of roughly 10 to 20 nm. Measurements to identify families must span several FSR and here will directly take advantage of the large wavelength range offered by the NV PSB.

In general, the multi-mode nature of these diamond microdisks results in dense PL spectra, making family identification challenging. However, a sparse spectrum in Fig.5.2, presumably from taper positioning that favors a specific family of modes, lends itself to analysis. The FSR measured for resonances in this spectrum are plotted in Fig. 5.2(b), along with FDTD (MEEP) simulated values. The measured data are significantly higher than FSR simulated for the fundamental TE$_{00}$ and TM$_{00}$ modes. With uncertainty in radius on the order of 10nm (EBL resolution) and uncertainty in thickness $\sim 10^2$nm (RIE-defined, estimated via SEM), the disagreement between measured FSR and that simulated for the fundamental microdisk modes cannot be explained by fabrication imperfections. This point is emphasized by additional simulations in Fig. 5.2(b), which account for possible disk dimension error. The large amplitude resonances in Fig. 5.2(a) therefore do not appear to be fundamental modes.

As alluded to by the typically dense mode spectra, simulations confirm that for the dimensions of these microdisks high-Q modes of both higher radial and vertical order exist. As radial(vertical)

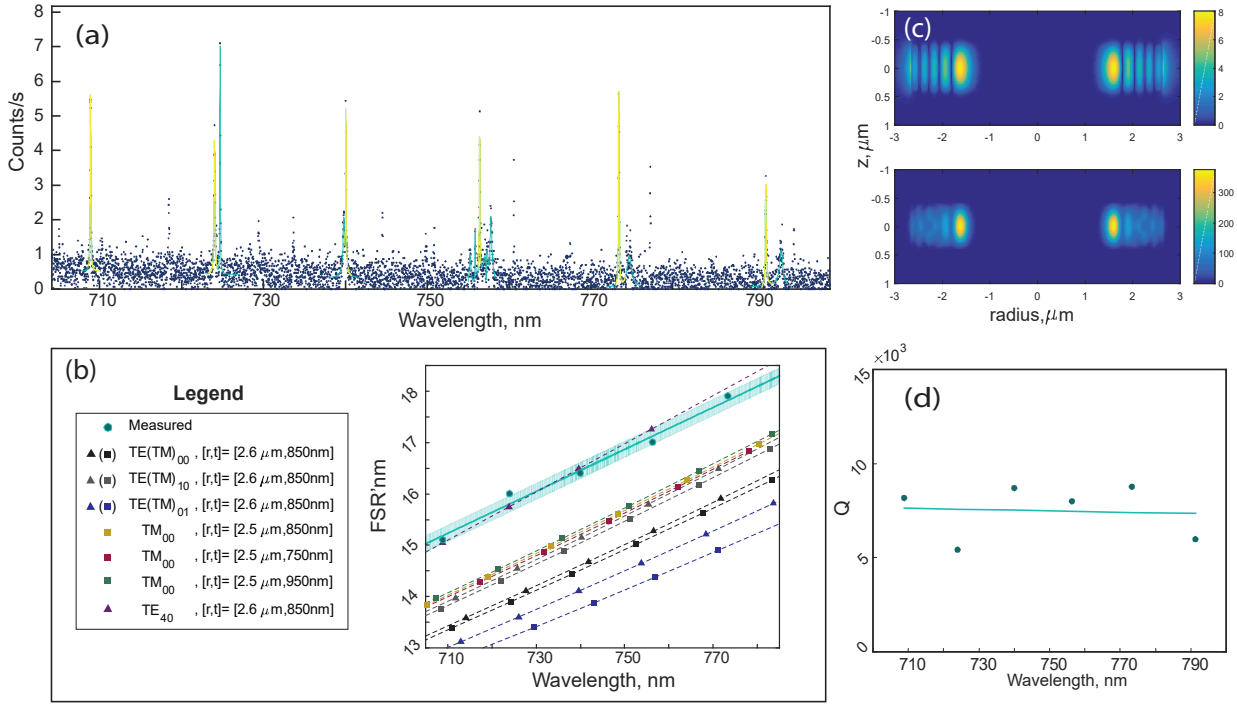

Figure 5.2: (a) PL from a [r,h]=[2.6μm, 850nm] disk. Blue lines: multiple-lorentizian fits. Yellow line (overlain): resonances hand-selected as part of the same family, based upon FSR. (b) Measured and simulated $FSR = \lambda_m - \lambda_{m+1}$ plotted as a function of λ_{m+1}. Teal line - linear fit; teal shading - fit $\pm$ standard deviation of residuals.(c) Example profile of the TE_{40} mode. The top panel: electric field in the radial direction. Bottom pannel: total field squared.(d) Q for yellow resonance fits in (a) as a function of wavelength.

Mode	λ_0	m_{ideal}/m
TM_{00}	738	0.58
TE_{00}	742	0.59
TE_{40}	741	0.91

Table 5.2: Comparison of radial mode m to the ideal value for fiber-taper coupling, for select resonances near 740nm.

order increases, the effective radius decreases(increases) and FSR as a function of wavelength increases(decreases). Consistent with these trends, the TE_{40} mode FSR is found to be of similar magnitude to measured values, despite a higher slope. In accordance with the observation that measured Q (Fig. 5.2(d)) of average $Q_{avg} = 7.4 \times 10^3$ shows no wavelength dependence, the TE_{40} family has simulated $Q_{rad} > 10^5$, confirming that the measured resonances are not radiation limited.

It is not immediately clear why higher order modes exhibit preferential fiber taper coupling, though a possibility is that phase-matching requirements are not being met by the fundamental microdisk modes. For fiber taper position defined by radial, ρ, and azimuthal, ϕ, coordinates with respect to the microdisk center, a taper with propagation factor β_f has electric field varying by exp(-$i\beta_f \rho sin(\phi)$). For a microdisk of mode field varying as exp($im\phi$), the phase matching requirement is $m \sim \beta_f r$[37].

Assuming the fiber has a waist radius expected for single mode fiber at 640nm[39], and evaluating the approximate β_f[39] for the wavelengths studied here at $\sim 740nm$ an m_{ideal} of $\sim$27 is required for ideal phase-matching. Table 5.2 demonstrates that while the fundamental modes show nearly twice the desired angular momentum, the higher order mode has m close to m_{ideal} and therefore phase matching could explain the preferential coupling. While it is standard to couple to microdisk modes demonstrating $m \sim 2 \times m_{ideal}$[37], in such instances the devices have been made extremely thin to relax phase matching requirements by boosting the intensity of the microdisk field that interacts with the fiber taper. Table 5.3 shows that the normalized disk thickness, $\tilde{t} = t/\lambda$, of the microdisks here is over twice the value of other devices. This is consistent with stringent phase-matching requirements limiting the coupling to lower-order modes in our system.

Material	λ_o (nm)	t (nm)	$\tilde{t}\left(\frac{\lambda_o}{n}\right)$
Si[41]	1550	344	0.8
GaP[32]	700	250	1.2
Diamond [62]	1550	940	1.4
Diamond (this paper)	735	850	2.8

Table 5.3: Comparison of device thickness normalized by the wavelength of study.

That higher-order modes demonstrate preferential coupling to the fiber taper further emphasizes that strong PL signals in the current fiber-taper microdisk system are not indicative of the best modes for Purcell enhancement, as these higher-order modes are also expected to have larger V. It therefore appears that the difference in PL intensity that cannot be explained by fiber collection for peaks in Fig. 5.1, is a consequence of number and efficiency of NVs coupling to each particular mode, rather than a result V_j.

5.3 Towards optimizing microdisks for emitter-photon coupling

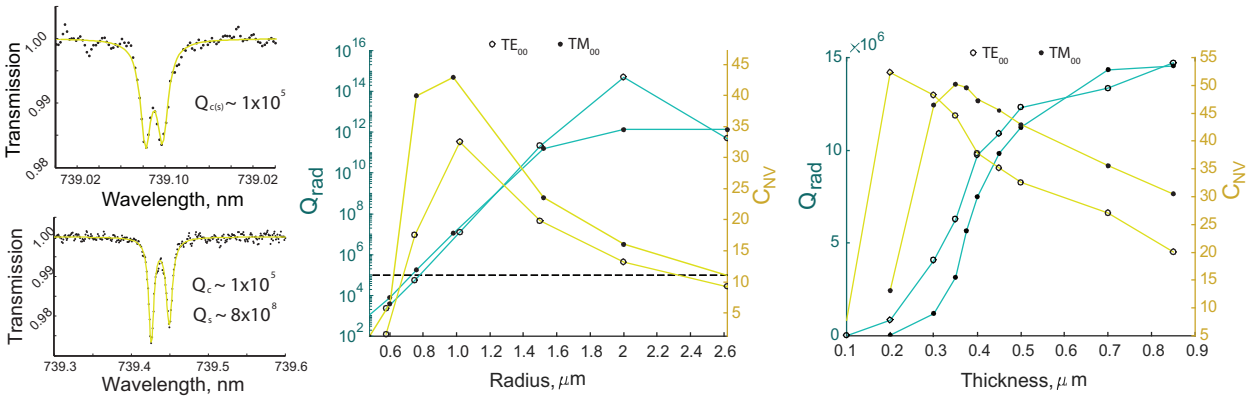

Figure 5.3: (a) Microdisk of [r,t]=[3.5,1]μm and (b) [r,t]=[3.6,1]μm, show highest-Q modes observed in diamond microdisks, as measured using a telecom fiber taper. (b) and (c) Simulated Q_{rad} and C_{NV} as a function of radius (c), with $t \sim 0.5\mu m$ and height (d), with $r \sim 1\mu m$. Connecting lines serve as a guide to eye. Dashed-dot line in (c) represents $Q_{rad} = 1 \times 10^5$.

By scaling microdisk dimensions down, it should be possible to simultaneously improve coupling to lower-order modes while decreasing V. Although Q_{rad} is also expected to decrease with microdisk r and t (Fig. 5.3(c) and (d), respectively), recall from Eqn. 2.6 that the intrinsic Q is

Ref	Geometry	Material	C_{zpl}	C_{NV}
[32]	Microdisk	GaP	20	0.6
[30]	PhC	Diamond	260	7.8
[25]	PhC	Diamond	1600	48
[26]	PhC	Diamond	1300	38

Table 5.4: Purcell factors calculated from cavity properties as reported in published literature.

practically limited by other contributions. We expect Q_{fab} to be the limiting contribution in Q, which in these diamond microdisks reaches $Q \sim 1 \times 10^5$ (Fig. 5.3(a) and(b)). This is the highest Q reported in SCD bulk resonators of which we are aware. As the role of imperfections in degrading Q increases as microdisks become smaller, 1×10^5 provides a realistic upper-limit on the Q_{fab} expected with our technique without further improvement in fabrication quality.

Intersection of the dashed and teal lines in Fig.5.3(c) indicates the radius at which degrading Q_{rad} will clearly influence the total Q. Assuming we are able to maintain current Q_{fab}, Fig. 5.3 (c) and (d) compare the theoretically realizable Purcell factor, C_{NV}, as a function of microdisk radius for an NV at cold temperatures, under optimal positioning and alignment ($\Theta, \eta = 1$):

$$C_{NV} = \zeta_{zpl} \frac{3}{4\pi^2} \frac{Q}{V} \tag{5.7}$$

where $\zeta_{zpl} = 0.03$ is the NV ZPL Debye Waller factor. C_{NV} would then be optimized by a disk with $r \sim 1\mu$m and $t \sim$400 nm. At $t \sim$ 400nm the devices will have $\tilde{t} = 1.4\lambda$, comparable to what is achieved when the current devices are measured at longer telecom wavelengths[62].

C_{NV}, as well as the emitter-independent value $C_{zpl} = C_{NV}/\zeta_{zpl}$, are presented in Table 5.4 for select literature values. With the results in Fig. 5.3(d) this demonstrates that if fabrication-related losses can be controlled diamond microdisks may be able to match the C_{NV} possible with other state-of-the-art on-chip devices, while providing a broader mode spectrum and direct low-loss coupling without integrated fiber couplers[60, 25].

Chapter 6

Conclusion and outlook

In this thesis, I have detailed the development of an integrated free-space-excitation, visible-fiber-taper collection setup that allows for deterministic PL collection from diamond microdisks. This setup removes many challenges that were faced with a free space collection approach.

With the setup in place, spectroscopy of SCD diamond microdisks was performed. Visible-wavelength fiber transmission measurements compared to complementary PL spectra demonstrate that spectral filtering by the fiber taper greatly affects the collection of cavity emission. Further PL spectroscopy, taking advantage of the PSB wavelength range to perform analysis over several FSR, suggests that there is a preferential coupling to higher order modes due phase matching restrictions.

By next fabricating thin devices it should be possible to relax phase matching requirements while lowering V, simultaneously removing higher-order vertical mode families and lowering the Q of higher-order radial modes. If fabrication losses can be controlled, smaller diamond microdisks may be able to achieve Purcell enhancements matching state-of-the-art diamond resonators, $C_{NV} \sim 50$, while providing broader mode spectrum and alternative integrated coupling options. The development of higher quality devices opens the door to improved coherent photon generation and collection for increasing, e.g., entanglement success rates.

Appendix A

Setup parts list

Table A.1: Parts list the setup including fiber-PL components and confocal options

Section	Piece	Vendor	Part No.	#	Comment
Purge Box	600mm rails	Thorlabs	XE 25L600/M	2	
	225mm rails	Thorlabs	XE 25L225/M	4	
	375mm rails	Thorlabs	XE 25L375/M	2	
	Connectors	Thorlabs	RM1G	4	Switched by workshop
	T-nuts	Thorlabs	1 XE25T1/M		For rails
	Angle Bracket	Thorlabs	AB90	5	Mounting box
	Plastic sheet	McMaster Carr	8560K357	1	And 8560K434
	Magnetic strip	McMaster Carr	5759K55	1	
	Latex cover	McMaster Carr	8633K32	1	
	Low-profile screws	McMaster Carr	92855A610		
	Tubing	McMaster Carr	5392K12		
	Push-to-connect fittings	McMaster Carr	Various		
	Flow meter	McMaster Carr	5084K24	1	
Objective Lens Control	Base Plate	Newport	9063-BM	1	Workshop adapted (holes)
	XY stages	Newport	UMR 8.25	2	
	Z stage	Newport	UMR 8.25A	1	Has aperature
	Stage actuators	Newport	BM17.25	3	
	XYZ Bracket	Workshop	NA	1	Custom, Aluminium
	Objective Bracket	Workshop	NA	1	Custom, Stainless Steel

Table A.1: Parts list the setup including fiber-PL components and confocal options

Section	Piece	Vendor	Part No.	#	Comment
	Mirror holder	Workshop	NA	1	Custom, for mirror XY stages, atop XYZ brkt.
	Lens Tube	Thorlabs	SM2L15	1	To help seal box w/ latex
	Lens Tube	Thorlabs	SM1L10	1	To bring Nikon CFI60 TU to focus on sample
	Thread Adapter	Thorlabs	SM1A12	1	M25x0.75 Thread. For, e.g., Nikon CFI60 TU mounting.
	Thread Adapter	Thorlabs	SM1A27	1	M26 thread adapter. For, e.g., Mitutoyo Plan Apo objectives
Breadboard	Breadboard	Newport	M-PG-23-2-ML	1	Raised, has microlocks.
	Breadboard	Newport	M-SA2-11	1	Small, inside box.
	Legs	Newport	M-XP-15	4	For raised breadboard.
Free space	Dichroic	Semrock	Di030R532-t1-25x36	1	
	Bandpass Filter	Semrock	FF01-532/3-25	1	
	Longpass Filter	Thorlabs	FGL590M	1-2	Remove green laser and Raman (collection, spectrometer)
	Longpass Filter	Thorlabs	FGL550	1	Remove green laser, keep Raman (collection)
	Lens tube	Thorlabs	SM1L03	1	for filter
	Mount	Thorlabs	LMR1/M	1	for bandpass
	Asphere	Thorlabs	AL1225M-A	1	Green Laser collimation

Table A.1: Parts list the setup including fiber-PL components and confocal options

Section	Piece	Vendor	Part No.	#	Comment
	Adapter	Thorlabs	SM1A6	1	Green laser asphere mount
	Package	Thorlabs	KT110/M	1	Free-space to fiber coupling
	Objective lens	Newport	M-10X	1	
	Beam splitter	Thorlabs	BS025	1	To be added
	Holder	Newport	UPA-CH1	1	To be added
	Motorized flip mount	Newport	8892-K-M	1	To be added
White Light	Lamp	Schott	A20500	1	
	Flex-light pipe	Navitar	1-60162	1	For co-axial connection
	Camera	Infinity	Infinity-LITEB	1	
	C-mount coupler	Navitar	1-6010	1	
	2X standard adaper	Navitar	1-6030	1	
	12X Ultra-zoom,3mm FF	Navitar	1-50503		
	Posts	Newport	9956-M	6	for mirrors and bandpass
	Spacers	Newport/ Thorlabs	Various		
Fiber Related	Z stage	Suruga	KZC06020-G	1	
	XY stage	Newport	460P-XY	1	
	XY Actuators	Newport	SM-25	2	
	Base plate	Newport/ workshop	9063-BM	1	
	Adapter plate	Newport	NA	1	For height as well as proper threads

Table A.1: Parts list the setup including fiber-PL components and confocal options

Section	Piece	Vendor	Part No.	#	Comment
Sample	90 degree bracket	Suruga	A47-3	1	For fiber holder
	Fiber holder base	Workshop	NA	1	
	Fiber holder	Workshop	NA	1	Was an un-used piece designed for different setup
	Translation stage	Newport	M-MR1.4	1	
	XY stage	Suruga	KYC6020-G	1	
	Stage controller	Suruga	DS102MS	2	One for fiber
	Link for controllers	Suruga	DS100-LINK2-0.5	1	
	Cable	Suruga	D214-2-2E	3	
	RS232C control cable	Suruga	D100-R9-2	1	
	Sample Holder	Workshop	NA	1	
	Goniometer	Suruga	B54-40UNR	1	
	Rotation Stage	Suruga	B43-60N	1	
	Base plate	Newport	9063-M	1	
	Adapater plate	Workshop	NA	1	

Appendix B

Setup notes and tips

- Vingetting occurs due to separation distance of objective and Nativar Zoom system. If future adjustments are made to setup, keep in mind to minimize this separation.

- To collimate a laser from its output coupler it is useful to reflect the beam to a far wall, using an additional mirror. Minimize spot size on the far wall with focusing optics and check that for distances near the setup, the beam width does not change.

- Rough alignment of the green laser on a chip substrate can be done by establishing two reference points - e.g. a pinhole in the beam path the objective lens entrance pupil. The farther away the points the better. Adjust one mirror for each reference point. Final alignment should be made by imaging the laser reflection from the substrate, using the CCD. A well-aligned beam is circular, with symmetric airy rings that preserve their symmetry as you focus the beam in and out.

- Every time a new sample is placed into the setup, the gonimeter must be adjusted to match the fiber. Place the sample in and ensure the chip is under the dimple. Bring the fiber down slowly, checking every so often that the sample is not contacted in a different spot on the taper by moving the sample stages in XY ($\sim 1\mu$m). If the fiber moves with the sample, it is contacted. Check which side it is contacted on, return your focus to the dimple, lift the fiber and adjust the goniometer. Iterate this process until the dimple touches the substrate first.

- For testing new devices or fibers it is effective to first touch the disks to ensure modes are present, without worrying about the loaded quality factor. It make take several hours to find a good position on the taper, and it is worth beginning with a

good device (e.g., GaP disks) to ensure you will see modes.

- Coulomb interactions between the fiber and the disk make it difficult to bring the fiber down slowly without contact. When trying a new fiber it can be helpful to contact the microdisk directly several times to find the optimal position along the taper. Next, lift the taper up, bring it down into focus and align it for the desired separation from the disk. After this, use a larger step size to bring the taper down quickly such that the edges of the taper contact the window substrate, holding it in position.

- When fiber pulling pay attention not only to efficiency, but the shape of the taper. Though the taper can be tensioned to make it straight, it is best to limit this. If the taper continues to "sag" during pulls, the torch position and height may need to be adjusted.

- Fibers mounted on a straight bracket may waiver from air currents. It is possible to turn off the nitrogen flow to attempt to mitigate this.

- Operate visible lasers near their maximum current for best performance.

- During PL collection there can be a large amount of green laser signal that is collected. We have found that the strong and broad signal creates an interference pattern that can show up on the spectrometer. Remove this with, e.g., a 590 LP filter in the path before the spectrometer entrance slit.

- Use mirrors B and C (Fig.4.1) to adjust the excitation path. Fine tune collection and white light paths using the mirrors associated with each path, which are decoupled from excitation.

- The free space collection path can be back-aligned as a first adjustment. Note that the beam splitter coatings do not work well near 735 nm and interference effects

will be present. Use the alignment laser or 637 nm laser, instead. For confocal imaging adjust until the beam is overlain with the green laser and shows desired symmetry. Final collection adjustments should be used with the beam splitter down, and collecting counts with the APD.

- After adjusting the objective bracket using the rails, use a level to ensure it is not angled after securing it.
- Take extreme care when moving the objective bracket that it does not hit the fiber. Any time you raise the objective above the box, be sure to cover the entrance aperature in the lid.

Appendix C

Permissions for Fig.1.2

Re: Permission request - SEM image - P. E. Barclay Group

Tamiko Masuda

Thu 4/19/2018 3:42 PM

To: Dirk Englund [redacted]

Thank you!

From: Dirk Englund [redacted]
Sent: Thursday, April 19, 2018 3:37:52 PM
To: Tamiko Masuda
Subject: Re: Permission request - SEM image - P. E. Barclay Group

sure, thanks Tamiko!

On Thu, Apr 19, 2018 at 11:35 PM Tamiko Masuda [redacted] wrote:

> Dear Dr. Englund,
>
> I am a Master's student in Paul Barclay's group at the University of Calgary and am hoping for your permission to use a couple wonderful SEM images from your papers.
>
> In particular, I have prepared the attached image (.jpg) to include in my thesis introduction. They are from:
>
> - S. Mouradian, N. H. Wan, T. Schröder and D. Englund. *Rectangular photonic crystal nanobeam cavities in bulk diamond.* Appl. Phys. Lett. (2017)
> - L. Li, T. Schröder, E. H. Chen, M. Walsh, I. Bayn, J. Goldstein, O. Gaathon, M. E. Trusheim, M. Lu, J. Mower, M. Cotlet, M. L. Markham, D. J. Twitchen and D. Englund. *Coherent spin control of a nanocavity-enhanced qubit in diamond.* Nat. Commun. (2015)
>
> If you could let me know whether or not this is alright with you, it would be kindly appreciated.
>
> Best regards,
> Tamiko

--
Dirk R. Englund
Associate Professor of Electrical Engineering and Computer Science
Massachusetts Institute of Technology
[redacted]

Re: Permission request - SEM image - P. E. Barclay Group

Andrei Faraon [redacted] >

Thu 4/19/2018 4:14 PM

To: Tamiko Masuda [redacted]

[redacted]

Yes, I approve.

Andrei

On Thu, Apr 19, 2018 at 2:28 PM Tamiko Masuda <[redacted]> wrote:

> Dear Dr. Faraon,
>
> I am a Master's student in Paul Barclay's group at the University of Calgary and am hoping for your permission to use a couple wonderful SEM images from your papers.
>
> In particular, I have prepared the attached image (.jpg) to include in my thesis introduction. They are from:
>
> - A. Faraon C. Santori, Z. H. K.-M. C. F. V. M. A. D. F. & Beausoleil, R. G. Quantum photonic devices in single-crystal diamond. *New J. Phys.,15*, 025010 (2013)
> - A. Faraon, C. Santori, Z. Huang, V. M. Acosta, and R. G. Beausoleil. Coupling of Nitrogen-Vacancy Centers to Photonic Crystal Cavities in Monocrystalline Diamond. *Phys. Rev. Lett.* 109 (2012)
>
> If you could let me know whether or not this is alright with you, it would be kindly appreciated.
>
> Best regards,
> Tamiko

--

Andrei Faraon

Assistant Professor of Applied Physics, Materials Science, and Medical Engineering
California Institute of Technology
[redacted]

Re: Permission request - SEM image - P. E. Barclay Group

Tamiko Masuda

Thu 5/3/2018 10:46 AM

To: Loncar, Marko [redacted]

Many thanks!

From: Loncar, Marko [redacted]>
Sent: Friday, April 27, 2018 12:09:00 PM
To: Tamiko Masuda
Subject: Re: Permission request - SEM image - P. E. Barclay Group

Hi Tamiko,

Of course. Go for it :).

Cheers,
Marko

On Apr 19, 2018, at 5:44 PM, Tamiko Masuda <[redacted] wrote:

Dear Dr. Loncar,

I am a Master's student in Paul Barclay's group at the University of Calgary and am hoping for your permission to use a couple wonderful SEM images from your papers.

In particular, I have prepared the attached image (.jpg) to include in my thesis introduction. They are from:

- M. J. Burek, Y. Chu, M. S. Z. Liddy, P. Patel, J. Rochman, S. Meesala, W. Hong, Q. Quan, M. D. Lukin and M. Loncar. *High quality-factor optical nanocavities in bulk single-crystal diamond.* Nat. Commun. 5 (2014)
- M. J. Burek, *et al. Fiber-Coupled Diamond Quantum Nanophotonic Interface* Phys. Rev. Appl. 8 (2017)

If you could let me know whether or not this is alright with you, it would be kindly appreciated.

Best regards,
Tamiko

<QVdevices_TM.jpg>

Bibliography

[1] P. Zoller, T. Beth, D. Binosi, R. Blatt, H. Briegel, D. Bruss, T. Calarco, J. I. Cirac, D. Deutsch, J. Eisert, A. Ekert, C. Fabre, N. Gisin, P. Grangiere, M. Grassl, S. Haroche, A. Imamoglu, A. Karlson, J. Kempe, L. Kouwenhoven, S. Kröll, G. Leuchs, M. Lewenstein, D. Loss, N. Lütkenhaus, S. Massar, J. E. Mooij, M. B. Plenio, E. Polzik, S. Popescu, G. Rempe, A. Sergienko, D. Suter, J. Twamley, G. Wendin, R. Werner, A. Winter, J. Wrachtrup, and A. Zeilinger, "Quantum information processing and communication," Eur. Phys. J. D **36**, 203–228 (2005).

[2] D. P. DiVincenzo, "The physical implementation of quantum computation," Fortschr. Phys. **48**, 771–783 (2000).

[3] H. J. Kimble, "The quantum internet," Nature **453**, 1023–1030 (2008).

[4] H. Kim, R. Bose, T. C. Shen, G. S. Solomon, and E. Waks, "A quantum logic gate between a solid-state quantum bit and a photon," Nat. Photonics **7**, 373 (2013).

[5] H. Bernien, B. Hensen, W. Pfaff, G. Koolstra, M. S. Blok, L. Robledo, T. H. Taminiau, M. Markham, D. J. Twitchen, L. Childress, and R. Hanson, "Heralded entanglement between solid-state qubits separated by three metres," Nature **497**, 86 (2013).

[6] N. Kalb, A. A. Reiserer, P. C. Humphreys, J. J. W. Bakermans, S. J. Kamerling, N. H. Nickerson, S. C. Benjamin, D. J. Twitchen, M. Markham, and R. Hanson, "Entanglement distillation between solid-state quantum network nodes," Science **356**, 928–932 (2017).

[7] A. Sipahigil, R. E. Evans, D. D. Sukachev, M. J. Burek, J. Borregaard, M. K. Bhaskar, C. T. Nguyen, J. L. Pacheco, H. A. Atikian, C. Meuwly, R. M. Camacho, F. Jelezko, E. Bielejec, H. Park, M. Lončar, and M. D. Lukin, "An integrated diamond nanophotonics platform for quantum optical networks," Science (2016).

[8] W. Pfaff, B. J. Hensen, H. Bernien, S. B. van Dam, M. S. Blok, T. H. Taminiau, M. J. Tiggelman, R. N. Schouten, M. Markham, D. J. Twitchen, and R. Hanson, "Unconditional quantum teleportation between distant solid-state quantum bits," Science **345**, 532–535 (2014).

[9] A. Sipahigil, M. L. Goldman, E. Togan, Y. Chu, M. Markham, D. J. Twitchen, A. S. Zibrov, A. Kubanek, and M. D. Lukin, "Quantum interference of single photons from remote nitrogen-vacancy centers in diamond," Phys. Rev. Lett. **108**, 143601 (2012;2011;).

[10] A. Sipahigil, K. D. Jahnke, L. J. Rogers, T. Teraji, J. Isoya, A. S. Zibrov, F. Jelezko, and M. D. Lukin, "Indistinguishable photons from separated silicon-vacancy centers in diamond," Phys. Rev. Lett. **113**, 113602 (2014).

[11] B. Hensen, H. Bernien, A. E. Drau, A. Reiserer, N. Kalb, M. S. Blok, J. Ruitenberg, R. F. L. Vermeulen, R. N. Schouten, C. Abelln, W. Amaya, V. Pruneri, M. W. Mitchell, M. Markham, D. J. Twitchen, D. Elkouss, S. Wehner, T. H. Taminiau, and R. Hanson, "Loophole-free bell inequality violation using electron spins separated by 1.3 kilometres," Nature **526**, 682 (2015).

[12] F. J. Heremans, C. G. Yale, and D. D. Awschalom, "Control of spin defects in wide-bandgap semiconductors for quantum technologies," Proceedings of the IEEE **104**, 2009–2023 (2016).

[13] V. A. Nadolinny, A. P. Yelisseyev, J. M. Baker, M. E. Newton, D. J. Twitchen, S. C. Lawson, O. P. Yuryeva, and B. N. Feigelson, "A study of 13 c hyperfine structure in the epr of nickel-nitrogen-containing centres in diamond and correlation with their optical properties," J. Phys. Condens. Matter **11**, 7357 (1999).

[14] M. K. Bhaskar, D. D. Sukachev, A. Sipahigil, R. E. Evans, M. J. Burek, C. T. Nguyen, L. J. Rogers, P. Siyushev, M. H. Metsch, H. Park, F. Jelezko, M. Lončar, and M. D. Lukin, "Quantum nonlinear optics with a germanium-vacancy color center in a nanoscale diamond waveguide," Phys. Rev. Lett. **118**, 223603 (2017).

[15] A. Zaitsev, *Optical Properties of Diamond: A Data Handbook* (Springer Science & Business Media, 2013).

[16] G. Balasubramanian, P. Neumann, D. Twitchen, M. Markham, R. Kolesov, N. Mizuochi, J. Isoya, J. Achard, J. Beck, J. Tissler, V. Jacques, P. R. Hemmer, F. Jelezko, and J. Wrachtrup, "Ultralong spin coherence time in isotopically engineered diamond," Nat. Mater. **8**, 383 (2009).

[17] G. D. Fuchs, G. Burkard, P. V. Klimov, and D. D. Awschalom, "A quantum memory intrinsic to single nitrogen-vacancy centres in diamond," Nat. Phys. **7**, 789 (2011).

[18] E. Neu, D. Steinmetz, J. Riedrich-Mller, S. Gsell, M. Fischer, M. Schreck, and C. Becher, "Single photon emission from silicon-vacancy colour centres in chemical vapour deposition nano-diamonds on iridium," New J. Phys. **13**, 025012 (2011).

[19] Y. N. Palyanov, I. N. Kupriyanov, Y. M. Borzdov, and N. V. Surovtsev, "Germanium: a new catalyst for diamond synthesis and a new optically active impurity in diamond," Sci. Rep. **5**, 14789 (2015).

[20] B. Pingault, D.-D. Jarausch, C. Hepp, L. Klintberg, J. N. Becker, M. Markham, C. Becher, and M. Atatre, "Coherent control of the silicon-vacancy spin in diamond," Nat. Commun. **8**, 15579 (2017).

[21] P. Siyushev, M. Metsch, A. Ijaz, J. M. Binder, M. K. Bhaskar, D. D. Sukachev, A. Sipahigil, R. E. Evans, C. T. Nguyen, M. D. Lukin, P. R. Hemmer, Y. N. Palyanov, I. N. Kupriyanov, Y. M. Borzdov, L. J. Rogers, and F. Jelezko, "Optical and microwave control of germanium-vacancy center spins in diamond," Phys. Rev. B **96**, 081201 (2017).

[22] A. D. Greentree, B. A. Fairchild, F. M. Hossain, and S. Prawer, "Diamond integrated quantum photonics," Mater. Today **11**, 22 – 31 (2008).

[23] I. Aharonovich, S. Castelletto, D. A. Simpson, A. D. Greentree, and S. Prawer, "Photophysics of chromium-related diamond single-photon emitters," Phys. Rev. A **81**, 043813 (2010).

[24] I. Aharonovich, S. Castelletto, B. C. Johnson, J. C. McCallum, D. A. Simpson, A. D. Greentree, and S. Prawer, "Chromium single-photon emitters in diamond fabricated by ion implantation," Phys. Rev. B **81**, 121201 (2010).

[25] M. J. Burek, C. Meuwly, R. E. Evans, M. K. Bhaskar, A. Sipahigil, S. Meesala, B. Machielse, D. D. Sukachev, C. T. Nguyen, J. L. Pacheco, E. Bielejec, M. D. Lukin, and M. Lončar, "Fiber-coupled diamond quantum nanophotonic interface," Phys. Rev. Applied **8**, 024026 (2017).

[26] S. Mouradian, N. H. Wan, T. Schrder, and D. Englund, "Rectangular photonic crystal nanobeam cavities in bulk diamond," Appl. Phys. Lett. **111**, 021103 (2017).

[27] M. J. Burek, Y. Chu, M. S. Z. Liddy, P. Patel, J. Rochman, S. Meesala, W. Hong, Q. Quan, M. D. Lukin, and M. Lonar, "High quality-factor optical nanocavities in bulk single-crystal diamond," Nat. Commun. **5**, 5718 (2014).

[28] A. Faraon, C. Santori, Z. Huang, K.-M. C. Fu, V. M. Acosta, D. Fattal, and R. G. Beausoleil, "Quantum photonic devices in single-crystal diamond," New J. Phys. **15**, 025010 (2013).

[29] L. Li, T. Schrder, E. H. Chen, M. Walsh, I. Bayn, J. Goldstein, O. Gaathon, M. E. Trusheim, M. Lu, J. Mower, M. Cotlet, M. L. Markham, D. J. Twitchen, and D. Englund, "Coherent spin control of a nanocavity-enhanced qubit in diamond," Nat. Commun. **6**, 6173 (2015).

[30] A. Faraon, C. Santori, Z. Huang, V. M. Acosta, and R. G. Beausoleil, "Coupling of nitrogen-vacancy centers to photonic crystal cavities in monocrystalline diamond," Phys. Rev. Lett. **109**, 033604 (2012).

[31] K.-M. C. Fu, C. Santori, P. E. Barclay, I. Aharonovich, S. Prawer, N. Meyer, A. M. Holm, and R. G. Beausoleil, "Coupling of nitrogen-vacancy centers in diamond to a gap waveguide,"

Appl. Phys. Lett. **93**, 234107 (2008).

[32] P. E. Barclay, K.-M. C. Fu, C. Santori, and R. G. Beausoleil, "Chip-based microcavities coupled to nitrogen-vacancy centers in single crystal diamond," Appl. Phys. Lett. **95**, 191115 (2009).

[33] P. E. Barclay, K.-M. C. Fu, C. Santori, A. Faraon, and R. G. Beausoleil, "Hybrid nanocavity resonant enhancement of color center emission in diamond," Phys. Rev. X **1**, 011007 (2011).

[34] A. Faraon, P. E. Barclay, C. Santori, K.-M. C. Fu, and R. G. Beausoleil, "Resonant enhancement of the zero-phonon emission from a colour centre in a diamond cavity," Nat. Photonics **5**, 301 (2011).

[35] M. J. Burek, N. P. de Leon, B. J. Shields, B. J. M. Hausmann, Y. Chu, Q. Quan, A. S. Zibrov, H. Park, M. D. Lukin, and M. Lonar, "Free-standing mechanical and photonic nanostructures in single-crystal diamond," Nano Lett. **12**, 6084–6089 (2012). PMID: 23163557.

[36] B. Khanaliloo, A. C. H. M. Mitchell, and P. E. Barclay, "High-q/v monolithic diamond microdisks fabricated with quasi-isotropic etching," Nano Lett. **15**, 5131–5136 (2015). PMID: 26134379.

[37] M. Borselli, "High-q microresonators as lasing elements for silicon photonics," Ph.D. thesis, California Institute of Technology (2006).

[38] K. Srinivasan, "Semiconductor optical microcavities for chip-based cavity qed," Ph.D. thesis, California Institute of Technology (2006).

[39] A. Yariv and P. Yeh, *Photonics: Optical electronics in modern communications. 6th edition* (Oxford University Press, 2007).

[40] K. J. Vahala, "Optical microcavities," Nature **424**, 839 (2003).

[41] M. Borselli, K. Srinivasan, P. E. Barclay, and O. Painter, "Rayleigh scattering, mode coupling, and optical loss in silicon microdisks," Appl. Phys. Lett. **85**, 3693–3695 (2004).

[42] M. Borselli, T. J. Johnson, and O. Painter, "Beyond the rayleigh scattering limit in high-q silicon microdisks: theory and experiment," Opt. Express **13**, 1515–1530 (2005).

[43] S. M. Spillane, T. J. Kippenberg, O. J. Painter, and K. J. Vahala, "Ideality in a fiber-taper-coupled microresonator system for application to cavity quantum electrodynamics," Phys. Rev. Lett. **91**, 043902 (2003).

[44] A. Meldrum, P. Bianucci, and F. Marsiglio, "Modification of ensemble emission rates and luminescence spectra for inhomogeneously broadened distributions of quantum dots coupled to optical microcavities," Opt. Express **18**, 10230–10246 (2010).

[45] A. Yariv, *Quantum electronics* (Wiley, New York, 1988), 3rd ed.

[46] M. Fox, *Quantum Optics: An Introduction* (OUP Oxford, 2006).

[47] K.-M. C. Fu, C. Santori, P. E. Barclay, L. J. Rogers, N. B. Manson, and R. G. Beausoleil, "Observation of the dynamic jahn-teller effect in the excited states of nitrogen-vacancy centers in diamond," Phys. Rev. Lett. **103**, 256404 (2009).

[48] M. W. Doherty, N. B. Manson, P. Delaney, and L. C. L. Hollenberg, "The negatively charged nitrogen-vacancy centre in diamond: the electronic solution," New J. Phys. **13**, 025019 (2011).

[49] M. W. Doherty, N. B. Manson, P. Delaney, F. Jelezko, J. Wrachtrup, and L. C. Hollenberg, "The nitrogen-vacancy colour centre in diamond," Phys. Rep. **528**, 1 – 45 (2013). The nitrogen-vacancy colour centre in diamond.

[50] B. H. Bransden and C. J. Joachain, *Physics of atoms and molecules* (Prentice Hall, New York;Harlow, England;, 2003), 2nd ed.

[51] C. Santori, D. Fattal, and Y. Yamamoto, *Single-photon devices and applications* (Wiley-VCH, Weinheim, 2010).

[52] R. Albrecht, A. Bommer, C. Deutsch, J. Reichel, and C. Becher, "Coupling of a single nitrogen-vacancy center in diamond to a fiber-based microcavity," Phys. Rev. Lett. **110**, 243602 (2013).

[53] J. Riedrich-Mller, C. Arend, C. Pauly, F. Mcklich, M. Fischer, S. Gsell, M. Schreck, and C. Becher, "Deterministic coupling of a single silicon-vacancy color center to a photonic crystal cavity in diamond," Nano Lett. **14**, 5281–5287 (2014). PMID: 25111134.

[54] R. Betzholz, J. M. Torres, and M. Bienert, "Quantum optical master equation for solid-state quantum emitters," Phys. Rev. A **90**, 063818 (2014).

[55] A. Auffèves, J.-M. Gérard, and J.-P. Poizat, "Pure emitter dephasing: A resource for advanced solid-state single-photon sources," Phys. Rev. A **79**, 053838 (2009).

[56] A. Auffèves, D. Gerace, J.-M. Gérard, M. F. m. c. Santos, L. C. Andreani, and J.-P. Poizat, "Controlling the dynamics of a coupled atom-cavity system by pure dephasing," Phys. Rev. B **81**, 245419 (2010).

[57] H. Carmichael, *Statistical methods in quantum optics 1: master equations and Fokker-Planck equations* (Springer-Verlag, New York, 1999).

[58] L. Childress and M. Lukin, "Modern atomic and optical physics ii," Lecture Notes.

[59] F. Graham-Smith and T. A. King, *Optics and photonics: an introduction* (Wiley, New York;Chichester;, 2000).

[60] C. P. Michael, M. Borselli, T. J. Johnson, C. Chrystal, and O. Painter, "An optical fiber-taper probe for wafer-scale microphotonic device characterization," Opt. Express **15**, 4745–4752 (2007).

[61] R. Ulrich and A. Simon, "Polarization optics of twisted single-mode fibers," Appl. Opt. **18**, 2241–2251 (1979).

[62] M. Mitchell, B. Khanaliloo, D. P. Lake, T. Masuda, J. P. Hadden, and P. E. Barclay, "Single-crystal diamond low-dissipation cavity optomechanics," Optica **3**, 963–970 (2016).